TÉCNICO LISBOA

Dosimetric comparison between proton and carbon ion beams for oncological treatments using Monte Carlo methods

Carlos Eduardo Vieira da Silva Correia

Thesis to obtain the Master of Science Degree in

Engineering Physics

Supervisor(s): Prof. Dr. Maria Teresa Haderer de la Peña Stadler
Dr. Isabel Augusta Pinheiro de Almeida

Examination Committee

Chairperson: Prof. Dr. Mário João Martins Pimenta
Supervisor: Dr. Isabel Augusta Pinheiro de Almeida
Member of the Committee: Prof. Dr. Patrícia Carla Serrano Gonçalves

December 2020

Acknowledgments

First and foremost I would like to thank my supervisors, Isabel Almeida and professor Teresa Penã, for their guidance during the development of this thesis, the dissertation would not have been possible without their support.

I would also like to thank Ana Cravo Sá from C2TN.

To my family for their support during these 5 years, especially my parents who provided financial and emotional help whenever needed.

I would also like to thank my colleagues, Filipe Mendes, my lab partner who shared the pains and anguishes of late night report writing. Gonçalo Raposo for listening to my rants about how ”Shaman is too strong in Hearthstone” and others of the sort as well as providing feedback for this document. Rafael Boto and Tiago Fernandes for always being available to answer endless amounts of questions about the courses. And to anyone else whose path crossed with mine throughout these last 5 years.

And finally a very special thank you to my best friend João Tiago for always being there for me whenever I needed not only during these past 5 years but since I can remember.

Resumo

A radioterapia é um dos principais métodos de tratamento para o cancro, o foco na radioterapia com protões ou carbono tem crescido na última década. As propriedades da radioterapia com partículas permitem uma distribuição de dose específica, erros no alcance das partículas podem levar a sobdosagem no tumor ou sobredosagem em orgãos saudáveis.

Este trabalho tem como objetivo quantificar as diferenças no alcance causadas pela incorrecta segmentação dos tecidos de um paciente, através da tomografia computorizada (CT). Perfis de dose foram obtidos utilizando o software de Monte Carlo (MC) TOolkit for PArticle Simulation (TOPAS). Os parâmetros para o plano foram optimizados com um código *open source* baseado em MATLAB, matRad. Os feixes foram validados com diferença média no alcance de (0.4 ± 0.3) mm.

Desenvolveu-se um plano de tratamento para um tumor cerebral de um paciente pediátrico. Introduziram-se erros na segmentação do tecido alterando o método de conversão de Hounsfield Units (HU) da CT para densidades e composições. Os voxeis da CT com músculo ou tecido adiposo mantiveram a sua composição mas passaram a ter a densidade da água, tornando possível estudar o impacto da alteração da densidade no alcance.

A diferença média no alcance foi 3.5 mm (2.6 % do alcance) com um desvio padrão de 0.4 mm, este valor é o cenário mais pessimista.

O longo tempo de computação necessário não permitiu terminar os cálculos referentes ao carbono, mas tendo em conta a validação destes feixes, prevê-se que a diferença no alcance seja parecida ou inferior à calculada para protões.

Palavras-chave: Terapia com Protões, Terapia com Iões de Carbono, Incertezas no Alcance, Segmentações Incorretas em CT

Abstract

Radiotherapy is one of the main treatments for cancer. During the last decade, its focus has shifted towards proton or carbon radiotherapy. The properties of particle radiotherapy allow for a specific dose distribution, errors in the range of the particles can lead to underdosage to the tumour or overdosage to healthy organs.

This work aims at quantifying the differences in range caused by missassignment errors in the Computed Tomography (CT) of a patient. Dose profiles were obtained using Monte Carlo (MC) *software* TOolkit for PArticle Simulation (TOPAS) and the plan parameters were optimized using matRad, an open source code based on MATLAB. The beams were validated with an average range difference of (0.4 ± 0.3) mm.

A treatment for a brain tumour of a pediatric patient was developed. Segmentation errors were introduced by modifying the method of conversion from Hounsfield Units (HU) in the CT to densities and compositions. Voxels of the CT, either with muscle or adipose tissue, kept their composition but were assigned the density of water. This allows the study of the impact of changes on the density on the range.

The average difference in range was 3.5 mm (2.6 % of the range) with a standard deviation of 0.4 mm, this is the worst case scenario.

The calculations regarding carbon radiotherapy could not be finished due to long computational times. Nevertheless taking into account the validation and physics of these beams, the difference in range is expected to be similar or inferior to the one calculated for protons.

Keywords: Proton Therapy, Carbon Ion Therapy, Range Uncertainties, CT Missassignments

Contents

List of Tables

List of Figures

Chapter 1

Introduction

Cancer represents a group of diseases, which can affect any part of the human body. Cancer originates from the formation of abnormal cells within a tissue or organ, which happens due to interactions between an individual's genetic factors and external agents. These abnormal cells grow rapidly and beyond their supposed boundaries, they can invade adjacent parts of the body and consequently other organs or tissues, this process is known as metastasis [1].

In 2018 there were more than 18 million new instances of cancer worldwide and the disease lead to almost 10 million deaths [2]. Cancer, in 2018, ranked as the second leading cause of death worldwide [1]. These numbers are expected to rise to nearly 30 million new instances in 2040 leading to more than 16 million casualties.

Due to the increase in both new instances and fatalities caused by cancer, several therapies are used for treatment of the disease, namely surgery, radiotherapy and chemotherapy. All these therapies have the same end goal, destroying the cancer cells while trying to minimize the damage to healthy ones [3]. Radiotherapy as been estimated as being beneficial to about 50% of cancer patients [4].

In Portugal, in 2018 there were 58 thousand new cases of cancer and they lead to 29 thousand deaths. Currently, there is a 10.6% chance of dying of cancer before the age of 75, a higher indicator than the 9.7% of the neighbour Spain which has recently (opened 1 clinic in 2019 and another in 2020) started using proton radiotherapy, Portugal has not yet invested into this type of treatment, with higher chance of death in Portugal perhaps it's time to invest in particle radiotherapy [5] [6].

It is important to understand how different types of radiotherapy methods interact with the human body. All radiation therapies have the same underlying principle, delivering energy to the tumor by means of an ionizing radiation with the intent of destroying the cancer cells at DNA level. The goal is also the same, delivering the highest possible dose (section (2.2)) to the tumour while delivering a dose as low as possible to healthy tissues. What distinguishes them is the used particle and consequently the ways in which these particles interact with the human body.

Photons are massless particles. Their energy is deposited as the beam moves through the body. Because of this the dose delivered will decrease as the depth of penetration increases which causes the dose to be at its highest when the beam enters the body. Another consequence is that healthy tissues that are geometrically before the tumour would receive a dose higher than the tumour itself as can be seen in Figure 1.1. This problem can be tackled by irradiating the tumour at various angles and with several beams to try and preserve normal tissues. One of these techniques is Intensity modulated radiotherapy (IMRT), which is a very powerful state of the art photon therapy technique where several beams, each with non uniform intensity profiles, work together to achieve a dose distribution that molds itself to the tumour, multileaf collimators are used to do this since they can block the necessary beams to ensure the nonhomogeneous dose is delivered, this approach helps spare normal tissue [7]. Due to

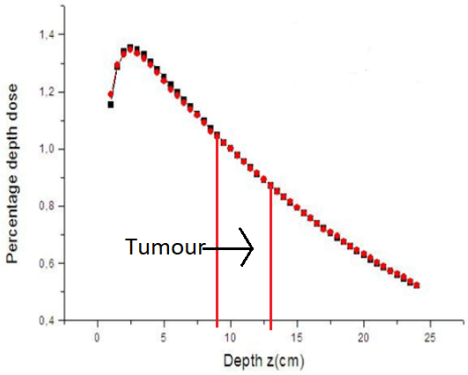

Figure 1.1:
Photon dose distribution in a water phantom.
Adapted from [9].

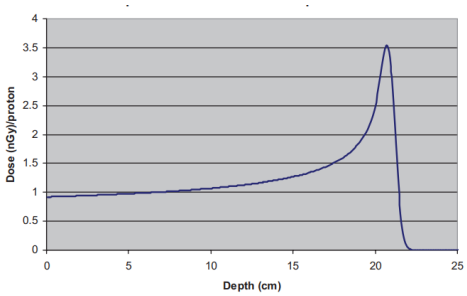

Figure 1.2:
Proton dose distribution showing the Bragg peak.
Adapted from [10].

the way photons interact with matter photon radiotherapy has intrinsic limitations.

In 1903, Bragg discovered that light charged particles deposit their energy in a different way. They deposit little energy during most of their path until finally they have a peak, before stopping, where they deposit most of their energy. This originates a well defined peak, known as the Bragg peak which is depicted in Figure 1.2. There are four main interactions protons, as charged particles, undergo. By inelastic Couloumb interactions with electrons, protons lose kinetic energy continuously as they move in a nearly straight line, this happen because the rest mass of protons is much higher than the one of electrons. Contrary to electron interactions, when a proton passes nearby a nucleus it will suffer a repulsive Couloumb collision that, since the nucleus mass is large, will cause a deflection in the proton's path. In nuclear reactions a proton will enter the nucleus which will then emit secondary particles, secondary protons, deuteron, triton, heavier ions as well as one or more neutrons[8]. Bremsstrahlung radiation is negligible at therapeutic proton beam energies.

Since the goal of proton therapy is to deliver dose in a very specific configuration errors in the range (section (2.6)) of the beams are much more severe than in photon radiotherapy. Therefore to accurately develop a treatment plan the effects that cause these uncertainties must be fully understood and quantified.

There are uncertainties inherent to the statistical nature of range and proton interactions, the incident beam is not monoenergetic, therefore the lower energy protons will have shorter range while higher energy protons will deposit their energy at a larger depth. Proton interactions with matter are governed by probability and the energy lost by each single proton will vary, these uncertainties are uncontrollable. Organ motion also has to be taken into account. This thesis focused on changes in the patients anatomy in the period between the planning of the treatment and the delivery and uncertainties in the CT numbers. Both of these errors cause missassignments in the tissues. In fact the material defined by the CT for a voxel of the patient will not be the actual material in that position.

Analytical methods also have errors due to heterogeneities, in the Bethe-Bloch equation ((2.1)) it can be seen that the loss of energy will depend on the characteristics, especially the density, of the traversed medium. The human body has several heterogeneities, for example a bone-soft tissue interface. The bone is denser so protons that travel through it will lose more energy and consequently deposit their energy at less depth and cause loss of sharpness of the SOBP, this happens because pencil beam scanning analytical methods don't consider the width of the beam when crossing tissues and therefore do not take the effects seen in Figure 1.3 into consideration.

In this work, Monte Carlo simulations were used so the heterogeneities errors mentioned above will

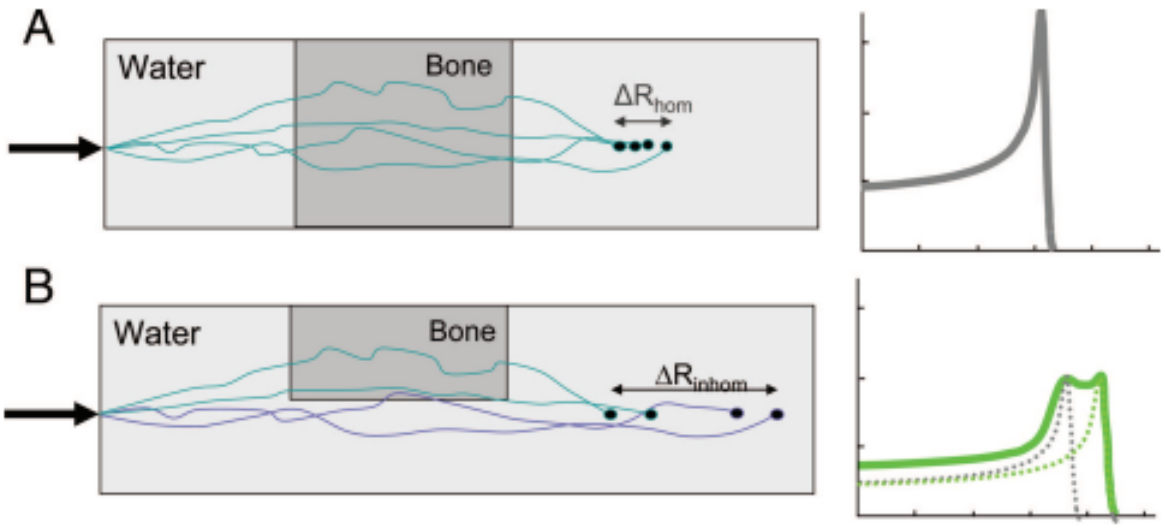

Figure 1.3: Effect of density heterogeneities in the Bragg peak. In case A all particles travel through similar structures while in case B some of the particles travel through bone while other don't, since bone is denser than water particles which travel without passing through the bone will lose less energy than the ones that do, particles that do interact with the bone will have lower range, this will lead to a widening of the Bragg peak. Adapted from [10].

not affect it since MC simulations take these effects into account.

Another difference between MC simulations and analytical methods is the entry dose, MC simulations consider scattering in the treatment head and therefore will have an higher entry dose when compared with analytical methods that do not take into account some of the particles as can be seen in Figure 1.4.

MC methods have similarities between them. Source of particles, treatment head (which includes all the machinery required to deliver the beam, range shifters, collimators, etc) and finally the patient itself must be modeled and all relevant particles must be tracked. Each particle is tracked by calculating its position at each step of the simulation and, considering the cross sections for all possible interactions (described in section 2.2.1), what interaction it will undergo, if any. Particles are tracked until their energy reaches a certain threshold and then deposit their energy in that position. MC simulations are inherently statistical, as are particle interactions with matter.

All simulations in this thesis were based on a Geant4 code [12], TOolkit for PArticle Simulation (TOPAS), developed by TOPAS MC Inc for particle therapy interactions and in close collaboration with particle therapy centers[13]. It is very important to mention that this code is for research purposes only.

Geant4 is a 4D simulation software that can handle time dependent variables, such as organ motion or moving components during treatment. TOPAS is a complex interface built on top of the of Geant4 libraries allowing TOPAS to evolve and derive from it[14].

One of the main advantages of TOPAS is that the user does not have to work with the underlying code, to run simulations it is only necessary to create parameter files, these parameter files specify all the variables of the simulation such as the geometry, source of particles, patient, and physics. TOPAS gives access to simple geometries which can be combined to create more complex structures, machinery specific components are also provided, this facilitates one's work as if more than one simulation is to be done with the same machinery the parameter file initializing geometry can be the same. To create the particle source it is necessary to define the parameters of the beam such as the chosen particle as well as its initial energy, and energy and angular spread. An important aspect of the simulation is the chosen physics setting, meaning what models the simulation will be based on to determine cross sections and probability of interactions as well as the energy cutoff. TOPAS has a default list that has been validated

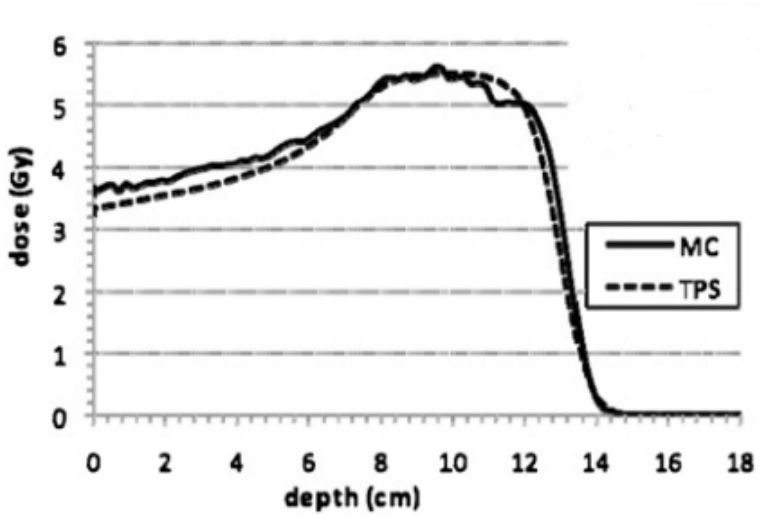

Figure 1.4: Difference in dose between a pencil beam scanning analytical model, Treatment Planning System, (TPS) and a Monte Carlo dose engine (MC). Adapted from [11].

for particle therapy applications[14] but the user can adjust it to their simulation if needed. Having defined all the above parameters the simulation can now be ran and the dose to each voxel (patient is split into voxels which are divisions of a chosen size each with their respective composition and density) is calculated, this is the scoring of the simulation.

Another capability of TOPAS which will be very useful for this work is the possibility of inheriting parameters from other files. This helps in keeping the files organized and facilitates the implementation. This feature will be discussed in more detail further ahead in the thesis.

The final goal of the work is to quantify the impacts of missassginment errors in the CT of a patient on the delivered dose in a treatment plan and infer about the clinically used margins. Too large margins lead to an unnecessary amount of normal tissue being irradiated. This work will also compare the results between proton and carbon ion radiotherapy and discuss the differences between the two as well as the advantages and disadvantages of each. As stated above TOPAS is very complex so starting with the simulation of a full treatment plan would not be a good idea, with this in mind the structure of the work will follow a pyramid structure, starting with generic more simple results and culminating in the complex development of a treatment plan while still analyzing and discussing the impacts of missassignments in every section.

Chapter 2

Concepts

2.1 Motivation

Radiotherapy has many concepts and their definitions are specific to the field. A difficult decision was made between explaining these concepts within the text as it would break the flow of the document for an experienced reader, or compiling them such that a non-expert could understand them. This chapter was the solution and presents the main concepts alongside a short explanation to serve as support for the reader throughout the thesis.

2.2 Dose

In radiotherapy dose is the amount of radiation in gray (Gy) which is delivered to a volume. In this work, dose refers to the dose distribution in a region of interest.

2.3 Region of interest

In the context of this thesis region of interest (ROI) is a volume to where the delivered dose must be monitored, this includes the targets volumes as well as organs at risk (OARs).

2.3.1 Target Volume

The three main volumes in radiotherapy are the Gross Tumour Volume (GTV), Clinical Target Volume (CTV) and Planning Target Volume (PTV), an example can be seen in Figure 2.1.

The GTV delineates the position and dimensions of the primary tumour.

The CTV encapsulates the GTV and delineates the extension of the tumour which cannot be imaged.

The PTV encapsulates both the GTV and CTV. The PTV is an extension of the CTV designed to take into account uncertainties in dose delivery which will be discussed later in this work.

2.3.2 OARs

Healthy tissues close to the PTV which are in danger of receiving enough dose to damage or destroy them, the treatment plan must be created taking this into account and should minimize the dose delivered to this regions.

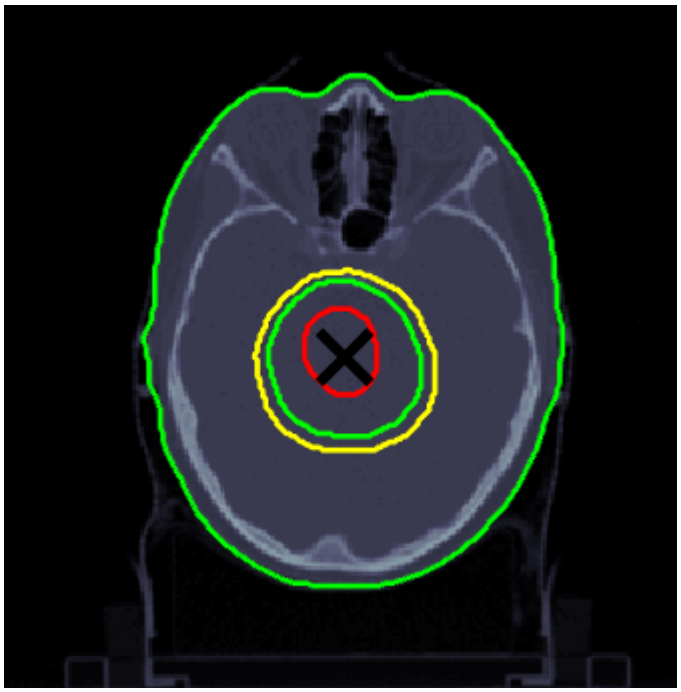

Figure 2.1: Gross Target Volume in red, Clinical Target Volume in green and Planning Target Volume in yellow.

2.4 Bragg Peak

In 1903 Bragg discovered that light charged particles deposit their energy in a different way, they deposit little energy during most of their path until finally they have a peak, before stopping, where they deposit most of their energy, this is know as the Bragg peak and can be seen in Figure 2.3.

2.5 Spread Out Bragg Peak

A single beams Bragg Peak is not sufficient to fully irradiate the tumour so multiple Bragg peaks must be combined to achieve a spread out Bragg peak (SOBP), illustrated in Figure 2.2 .

2.6 Range

The rate of which a beam loses energy can be calculated by the Bethe-Bloch equation

$$-\frac{1}{\rho}\frac{dE}{dx} = 4\pi N_A r_e^2 m_e c^2 \frac{Z}{A}\frac{z^2}{\beta^2}(ln\frac{2m_e c^2\gamma^2\beta^2}{I} - \beta^2 - \frac{\delta}{2} - \frac{C}{Z})(MeVcm^2g^{-1}) \tag{2.1}$$

where N_A is Avogadro's number, r_e is the electron classical radius, m_e is the rest mass of the electron, z is the charge of the beam particle, Z is the atomic number of the traversed material, A is the atomic weight of the traversed material, c is the speed of light, v is the velocity of the beam, $\beta = \frac{v}{c}$, $\gamma = \frac{1}{\sqrt{1-\beta^2}}$, I is the mean excitation potential of the traversed material, γ takes into account the density corrections when close electrons shield remote electrons, the effect will be a reduced energy loss at high energies, C is the term representing shell corrections at low energies.

Having calculated the stopping power we can calculate the range of the beam using the continuous

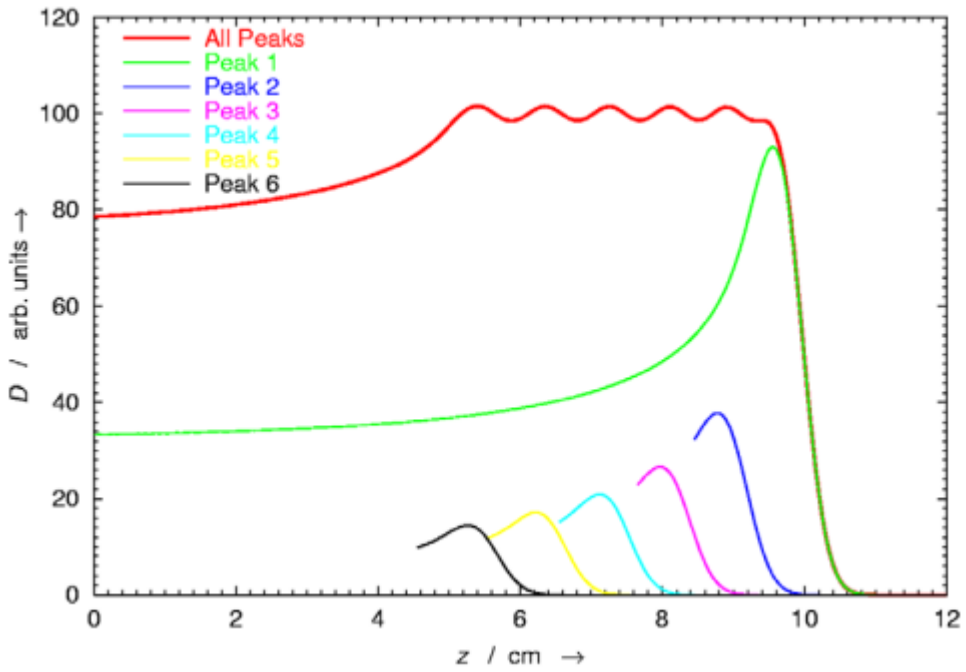

Figure 2.2: Dose distribution with Bragg peaks and their corresponding spread out Bragg peak for a water phantom. Reproduced from [8].

slowing down approximation (CSDA).

$$R(E_{ini}) = \int_0^{E_{ini}} (\frac{dE}{dx})^{-1} dE \tag{2.2}$$

It is important to keep in mind that both the energy loss and range are average quantities and are only calculated for a beam and not single particles.

2.6.1 R_{80}

There are several ways to define the range of a beam, but one of the most common ones used clinically worldwide is its R_{80}. R_{80} is defined as the range where the dose falls to 80% of its maximum as illustrated in Figure 2.3.

2.7 Full Width at Half Maximum

Full Width at Half Maximum (FWHM) is used to define the width of the Bragg Peak of a beam, it is defined as the distance between both sides of the peak where the dose is 50% of its maximum. Figure 2.3 shows how the FWHM is calculated.

2.8 Voxel

A voxel is the division, normally a small cube, of the patient/phantom in the CT as well as for the scorer in the simulations.

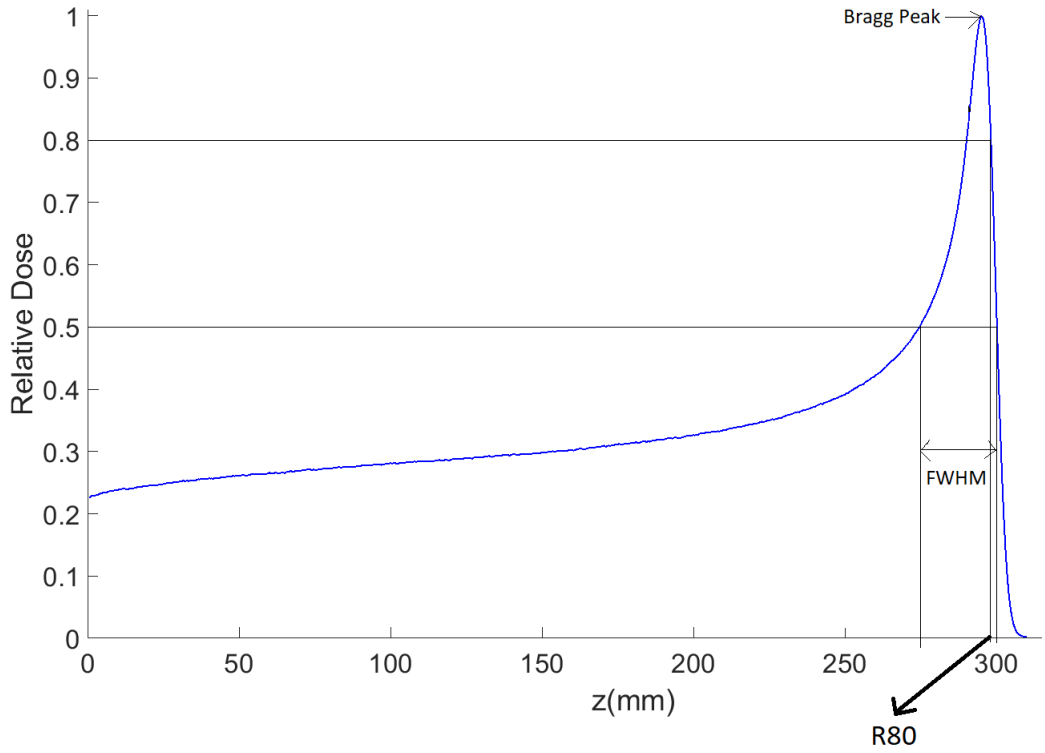

Figure 2.3: Bragg Peak, R_{80} and Full Width at Half Maximum (FWHM).

2.9 Beam Eye View

Beam Eye View (BEV) is utilized in radiotherapy as an imaging technique which helps the planning of the treatment by verifying whether the positioning of the patient is correct relative to the treatment head.

2.10 Lateral Penumbra

The lateral penumbra of a beam is its lateral sharpness. It depends on several factors such as the depth of penetration, composition of the traversed medium and characteristics of the beam itself like the used particle and energy.

2.11 Relative Biological Effectiveness

Relative Biological Effectiveness (RBE) is a measurement of how effective a radiation is at damaging cells in compparison to a reference, shortly it can be defined as the ratio of biological dose between two radiations with the same physical dose. A higher RBE means less dose is required to achieve the same damage to tissues. The reference is 1 for photons.

2.12 Hounsfield Units

The image in a CT is constructed by acquiring the profiles of transmission of X-rays passing trough a phantom/patient in various directions, these profiles are then converted into images of the phan-

tom/patient. The fluence of each X-ray is given by equation 2.3

$$\Phi(E) = \Phi_0(E) \times exp(-\int_0^l \mu(E,p)\,dp) \tag{2.3}$$

where $\mu(E,t)$ is the linear attenuation coefficient of the phantom/patient along the projection with length l at p position and is given by equation 2.4.

$$\mu(E) = \rho \times N_A \times \sum_{n=1}^{n} (\frac{w_i}{A_i} \times \sigma_i(E)) \tag{2.4}$$

where ρ is the density, N_A is the Avogadro number, w the element weight, A the atomic mass and σ the total cross section. The Hounsfield units are then given by equation 2.5

$$HU = (\frac{\mu}{\mu_{water}} - 1) \times 1000 \tag{2.5}$$

where HU is defined in a way that ensures that the value for water is always 0 and the value for air is always -1000.

Chapter 3

Generic Beams

3.1 Motivation

To get familiar with the complex MC simulation software TOPAS, a set of generic beams and different set of phantoms were defined and simulated. Especially the gained expertise and the created baseline for both TOPAS and MATLAB, where during this period a large set of varied MATLAB functions were developed, will help automatize and facilitate not only the creation of the necessary TOPAS parameter files but also the treatment and analysis of the results.

3.2 Setup

Simulations were ran for 3 different materials, water, water-like muscle and water-like adipose tissue. Water-like muscle and water-like adipose tissue are virtual materials that have the composition of muscle and adipose tissue (Table 3.1), respectively, but the density and mean excitation energy of water. The proton beam characteristics mirror the beam of the Maastricth therapy center in the Netherlands and are shown in Table 3.2.

The setup for the simulations can be seen in Figure 3.1, each beam travels trough a phantom divided into voxels with 0.5 mm in depth and 5 mm in both height and width, voxels in this section can be bigger since the behaviour of interest is the integrated depth/dose distribution, meaning for a particular depth the value of the dose is obtained by summing all the bins in width and height at this depth, this saves computational time as well as RAM usage (simulations were ran in a 4 threads and 16 GB of RAM computer). The energy used was 80 MeV, 120 MeV, 160 MeV, 200 MeV and 240 MeV, for each energy 500000 histories were split into 5 differently seeded 100000 history simulations, the simulations were split due to computational time reasons and the use of different seeds is for statistical purposes .

Material	Hydrogen	Carbon	Nitrogen	Oxygen	Sodium	Phosphorus	Sulfur	Chlorine	Potassium
Water	2			1					
Water-like muscle	0.102	0.143	0.034	0.71	0.001	0.002	0.003	0.001	0.004
Water-like adipose tissue	0.114	0.598	0.007	0.278	0.001		0.001	0.001	

Table 3.1: Composition of water, water-like muscle and water-like adipose tissue materials. Taken from the Geant4 database.

Parameter	Value
Type	Emittance
Distribution	BiGaussian
Energy Spread	0.3174
σ_x	2.2593950320 mm
σ'_x	0.0019356750827832650
Correlation$_x$	0.10735935090014787
σ_y	2.41228329 mm
σ'_y	0.00172599549557624
Correlation$_y$	-0.155731996511997262

Table 3.2: Parameters mirroring the beam from the Maastritch therapy center which will be used in the generic beam chapter.

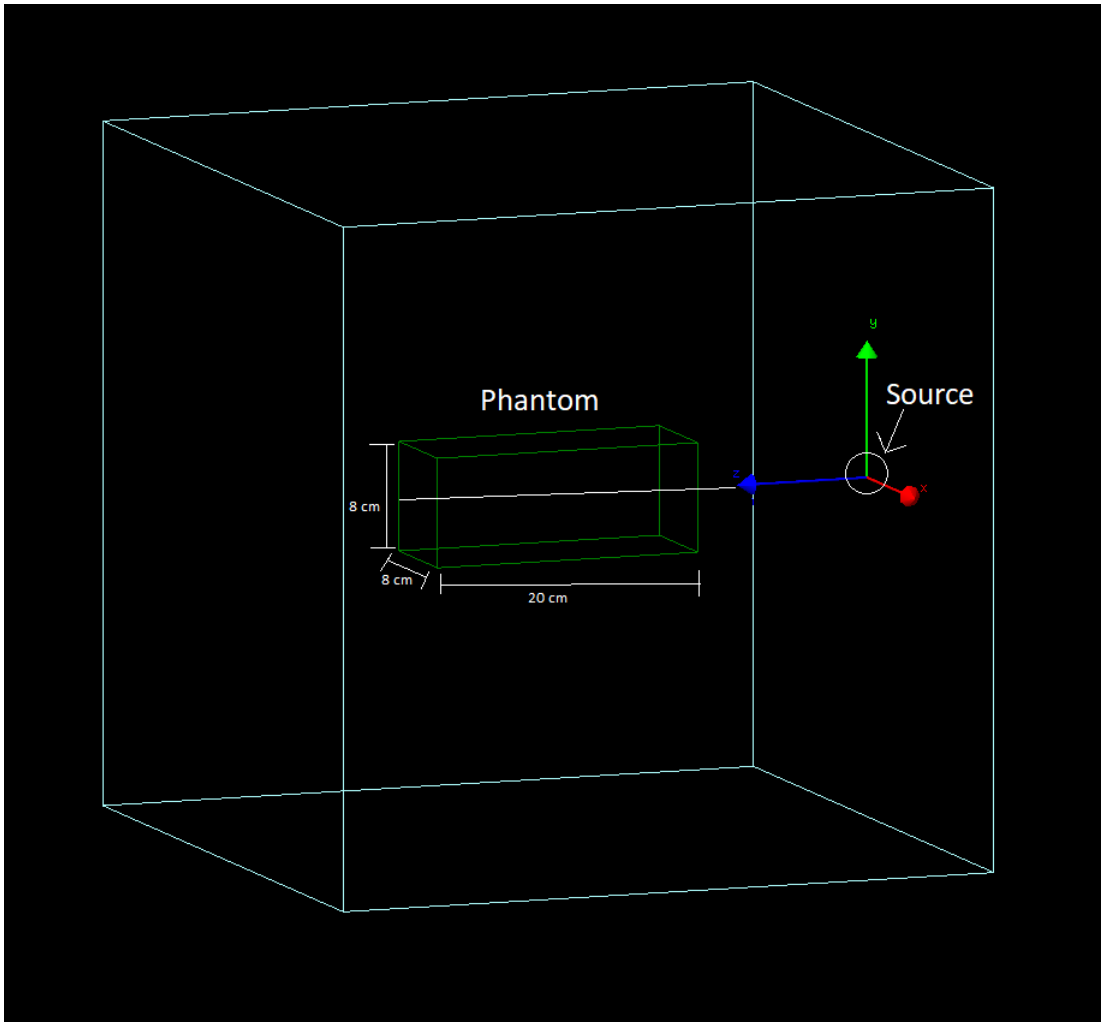

Figure 3.1: General setup for the simulations of different energies of generic beams.

Material	Energy(MeV)	R_{80}(mm)	FWHM(mm)	Δ R_{80}(%)	Δ FWHM(%)
Water	80	50.3	5.2	——	——
Water-like muscle	80	50.7	5.0	0.8	3.85
Water-like adipose tissue	80	50.0	4.8	0.6	7.7
Water	120	105.0	10.2	——	——
Water-like muscle	120	105.8	10.1	0.7	1.0
Water-like adipose tissue	120	104.6	10.0	0.5	2.0
Water	160	174.8	16.7	——	——
Water-like muscle	160	176.3	16.7	0.9	0.0
Water-like adipose tissue	160	174.3	16.5	0.3	1.2
Water	200	257.7	24.5	——	——
Water-like muscle	200	259.9	24.7	0.9	0.8
Water-like adipose tissue	200	257.0	24.2	0.3	1.2
Water	240	352.0	34.0	——	——
Water-like muscle	240	355.0	34.3	0.9	0.9
Water-like adipose tissue	240	351.1	34.0	0.3	0.0

Table 3.3: Range (R_{80}) and Full Width Half Maximum (FWHM) of the Bragg peak of proton beams of different energies in water, water-like muscle and water-like adipose tissue phantoms. Δ is the relative difference. Water-like muscle and water-like adipose tissue are, respectively, materials with the composition of muscle or adipose tissue but with the density and mean excitation energy of water.

3.3 Results

The goal is to obtain and analyze the integrated normalized depth/dose distribution with a heavy focus on the R_{80} and FWHM which are defined in sections (2.6) and (2.7), respectively. The output of the simulations in TOPAS is in DICOM (Digital Imaging and Communications in Medicine) format. To work the data, several MATLAB scripts were developed both as a way to transform the DICOM information into dose values and to plot the data and calculate the ranges or other relevant quantities, the MATLAB scripts developed in this section attempt to be as general as possible so that they can be used throughout the thesis. The expertise and functions developed in MATLAB were of extreme relevance ahead when the data became more complex to analyze and more technical aspects of MATLAB needed to be utilized the scripts.

The depth/dose for each of the 5 energies and 3 materials are shown in Figure 3.2 and the values for R_{80} as well as FWHM and their respective relative differences are in Table 3.3. It can be seen that the relative differences of R_{80} are lower than 1 % while the differences in FHWM fluctuate more in percentage but always stay below 0.3 mm. The absolute difference in range rises as the energy increases as it would be expected since the beam travels through a greater depth and the differences in material have a larger impact on the loss of energy. This results serve as a baseline in what to expect from the impacts of missassignments of tissues on the dose. The difference in R_{80} being smaller than 1% means that this error is within the margins considered by most clinics which administer proton therapy, these margins are 3.5% of the range plus 1 to 3 mm [15]. Having developed a baseline on what to expect from missassignment errors, an overall understanding of the TOPAS software and developed the required MATLAB scripts which allow the analysis of the data the next chapters will focus on the procedures needed to develop a treatment plan for a pediatric clinical case.

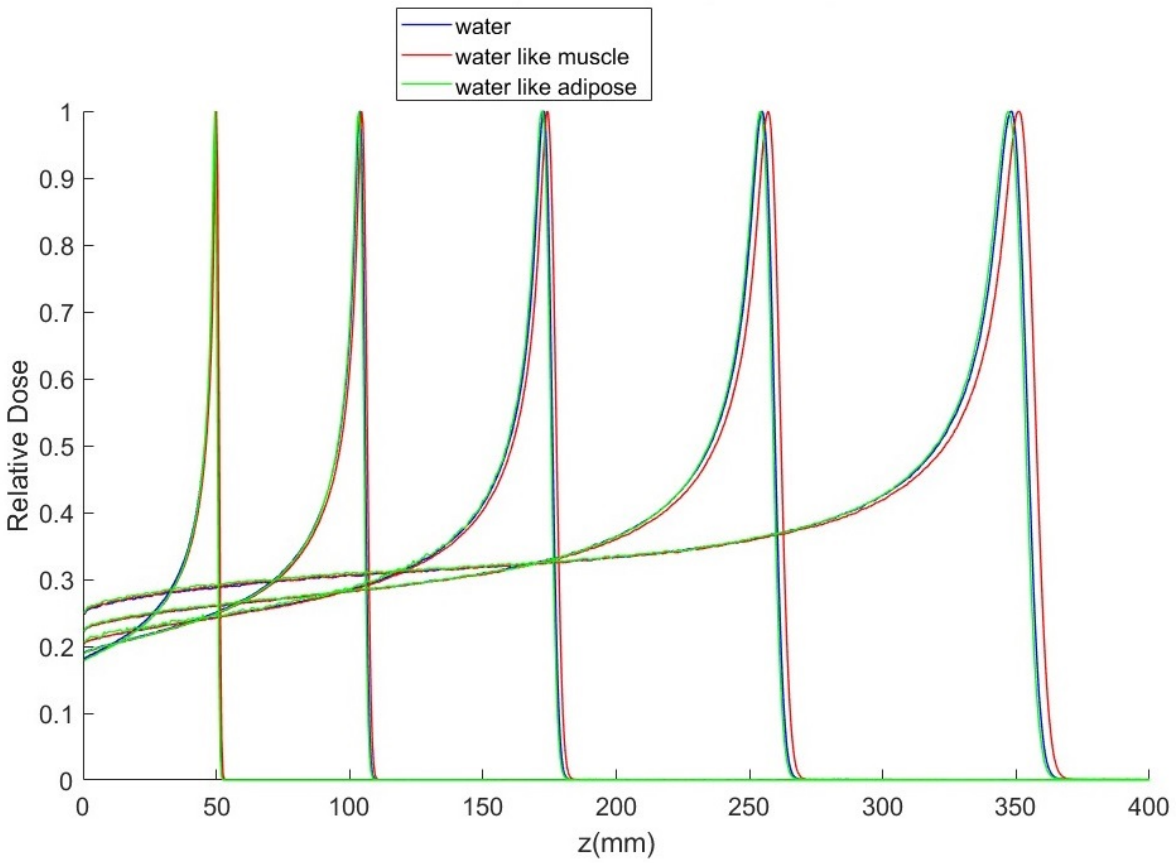

Figure 3.2: Normalized Depth/dose distributions for energies of 80 MeV, 120 MeV, 160 MeV, 200 MeV and 240 MeV, from left to right. Water-like muscle and water-like adipose tissue are, respectively, materials with the composition of muscle or adipose tissue but with the density and mean excitation energy of water.

Chapter 4

Validation

4.1 Motivation

The process of creating a treatment plan with particle therapy requires defining several parameters that follow detailed clinical protocols which depend on the type of particle, beam, machine and even center. In particular, the treatment plan is calculated by complex algorithms that manipulate parameters such as spot position and size as well as beam energy and weight to achieve the best possible dose to the target while minimizing dose delivered to the surrounding volumes.

In this thesis, an open-source research software named matRad developed by German Cancer Research Center in the Helmholtz association was used as a tool to create the treatment plan that would later be simulated with Monte Carlo dose engine. matRad is a *software* developed in MATLAB with a graphical user interface, shown in Figure 4.1, that allows the user to easily input a set of variables and parameters and gives a treatment plan as the final result. The full matRad flowchart can be seen in Figure 4.2. The first two variables, which can be imported, are the *cst* struct (RTsegmentation) which stores information about the regions of interest and the *ct* struct (RTct) that holds the CT of the phantom or pacient, having the Hounsfield units for each voxel as well as the resolution and dimensions, italic names refer to matRad variables. The next step is defining the treatment plan parameters, this information is stored in the *pln* struct (RTplan) and includes the chosen particle and machine for the treatment as well as the gantry and couch angles which are to be used, the separation between scanning spots and the type of optimization that will be ran further ahead. Using RTsegmentation, RTct and RTplan matRad generates the *stf* struct (RTspots) that holds information about the spacial distribution of the spots and the *dij* struct (RTdij) which contains the contributions to dose of each beam and the initial dose.

Finally, by inverse planning and iterative functions, the dose is optimized, taking into account the constraints and objectives set in RTplan, to achieve the minimum difference between planned and delivered dose. The result is stored in the *resultGUI* struct (RTresult) and contains the dose distribution as well as the weights to be used for each beam.

4.2 Single Beams

To be able to run the treatment plan created in matRad in TOPAS the beams in the matRad machine have to be validated, as explained here. The chosen machine consists of 86 generic beams with energies ranging from 73.4 MeV to 216.4 MeV corresponding to , accordingly, to ranges in water (R_{80}) of 44.97 mm to 298.84 mm covering clinical ranges. The dose distributions for each of these beams are calculated using the analytical model described in [16].

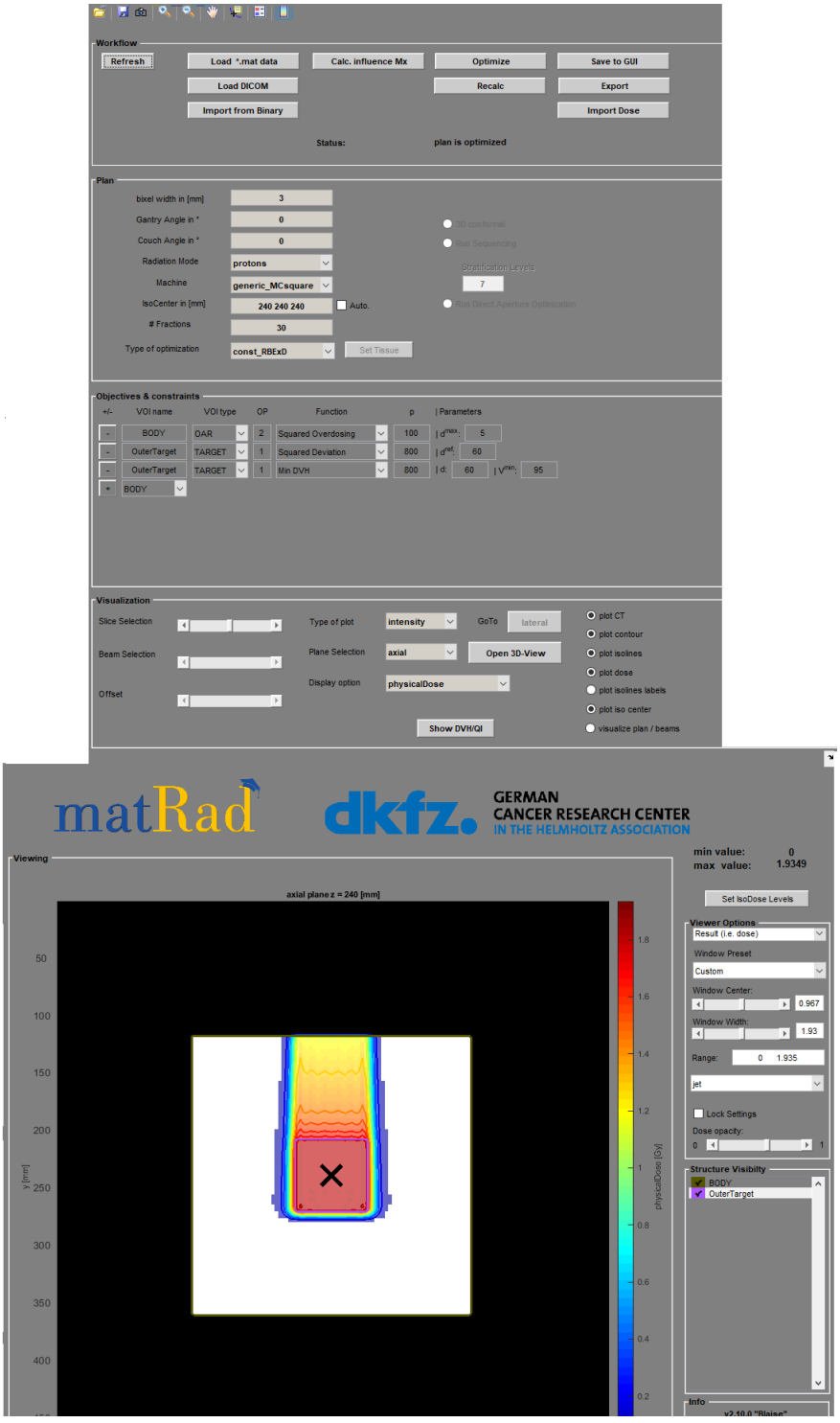

Figure 4.1: matRad graphical user interface.

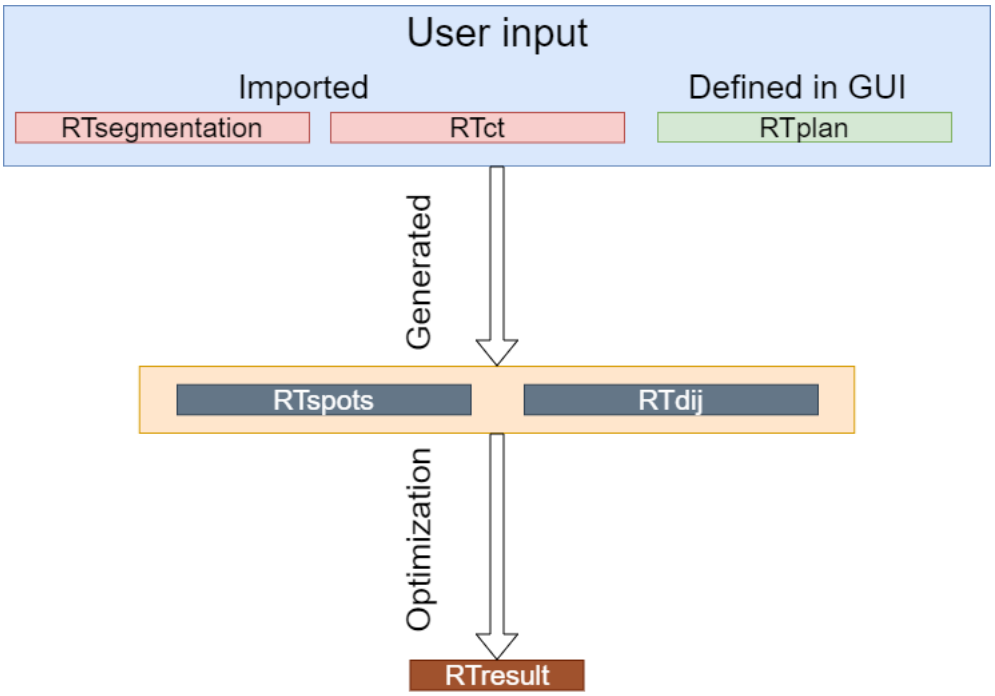

Figure 4.2: matRad flowchart for a treatment plan.

The validation consisted of simulating proton beams with no initial energy spread travelling through a cubic water phantom divided into 0.5 mm voxels, similar to Figure 3.1, the size of the phantom changed for each energy taking into account the necessary dimension to be able to score the relevant zones of the dose distribution (entrance, plateau, Bragg Peak and distal falloff) using TOPAS default physics settings and obtaining the integrated dose/depth distribution of each beam. This dose distribution is then compared with the one from corresponding beam in the matRad machine.

To adjust the beams, the energy was used as a free parameter and changed until the difference in range (R_{80}) from the simulated beams and the corresponding MatRad ones was smaller than 1 mm (2 voxels), although preferably errors would be within 0.5 mm (1 voxel). The process of reducing this difference is extremely time consuming and 1 mm is within the margins considered by clinics when creating a treatment plan, which are 3.5% of the range of the beam plus 1 to 3 mm (depending on the clinic) [15].Each beam simulation, similar to section (3.2), consisted of 5 separate simulations with different seeds and 1000000 histories each. 5 seeds were used not only to be able to calculate a standard deviation for the range and full width at half maximum of each peak but also to protect against any error that could happen during said simulations, by doing several smaller simulations if any error occurs only the current simulation will be affected instead of rendering an entire simulation useless if a single large one was ran, (some of the simulations take a long time to be completed and the computer used at the time could crash). The way in which the text files defining the parameters for the simulations were organized can be seen in Figure 4.3, the files were setup in a way that the only necessary change to be made to adjust the energy and repeat the simulation is a single parameter in the *Beam Parameter* file, the *Geral* file has the phantom, material, scorer and detector definitions which are the same for all 86 beam energies, (except for the phantom/scorer size as stated above) while the Beam Parameter file has the parameters for each beam (there are 86 of these) and the *Seeding* file defines the seed and the output file (5 of these for each of the 86 beams).

Table 4.1 displays the values of FWHM and R80 for each energy as well as their corresponding absolute difference (Δ) when compared to the corresponding beam in the matRad machine and in the final row the average values of Δ.

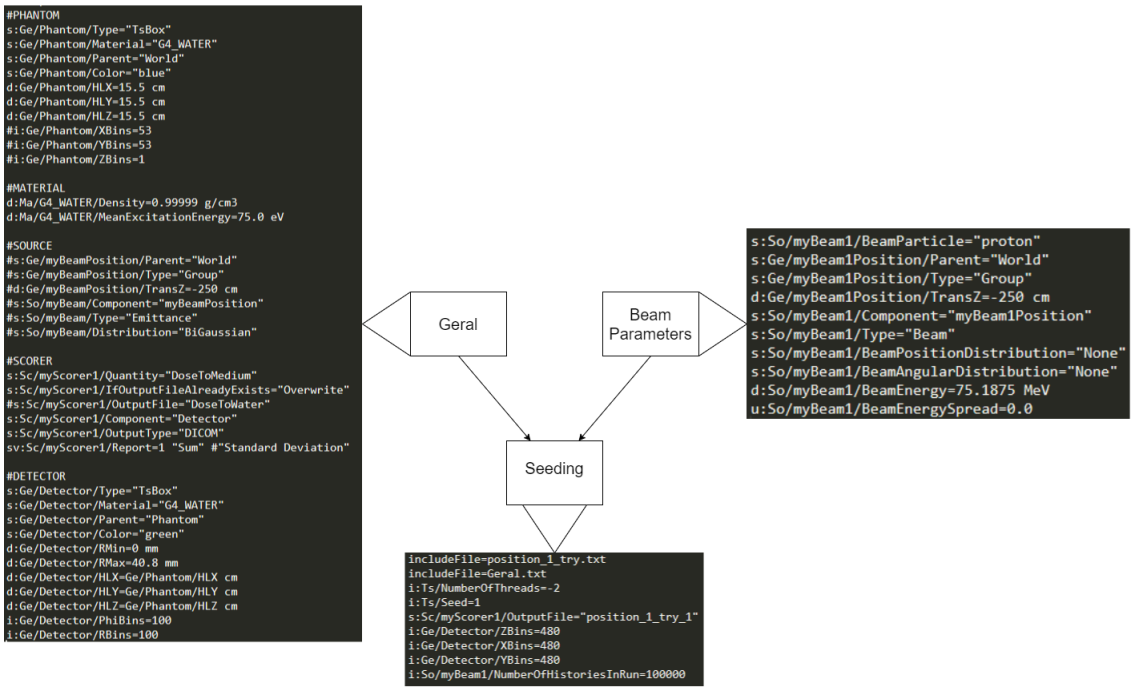

Figure 4.3: Flow chart of the organization of the parameter files for the simulation. The *Geral* file is common for all beams while the *Beam Parameters* and *Seeding* files are an example, in this case for the lowest energy in the matRad machine.

Figure 4.4 shows that at the Bragg Peak zone, both matRad and TOPAS beams are at close accordance which is excellent since this is the zone which will contribute the most to the total dose. Figure 4.5 shows that the largest difference between the matRad beams and their equivalent TOPAS beams occurs at the entrance and plateau regions, especially for lower energies. This occurs since, as mentioned in the introduction, Monte Carlo simulations take into account scattering at the treatment head while analytical methods don't and this causes analytical methods to "lose" some particles leading to lower dose at the entrance [11]. This is less of an issue than one would expect since this zone is less relevant to the overall plan. For lower energies it can, in a perfect scenario, influence a volume which is outside the patient and in the case that it influences the Planning Target Volume (PTV) there will be less particles and therefore a lower impact on the overall dose.

The average value of 0.4 mm for the difference in R80 between the matRad beams and the simulated ones along with Figure 2.3 prove that in the zone close to the Bragg Peak the dose distribution of matRad and TOPAS beams are at close accordance. Therefore the parameters calculated through matRad can be used to simulate treatment plans with TOPAS, in principle, without significant differences between the two.

4.3 Box Phantom

After achieving a satisfying level of agreement between TOPAS and matRad for dose distributions for single beams, the following step was to move to a target volume. This section intends to verify if multiple beams can be combined to achieve a specific dose distribution in a target volume. The simplest option is a constant dose in a cubic water phantom. For these simulations an example included in matRad files, which can be seen in Figure 4.6 was used. It consists of box phantom CT including a defined region of interest (ROI) and isocenter. The phantom is a 160x160x160 voxel cube with a 3 mm resolution making it a 480x480x480 mm^3 cube. The ROI is a smaller 240x240x240 mm^3 cube made of

Energy(MeV)	R80$_{\mathrm{MC}}$	R80$_{\mathrm{mR}}$(mm)	Δ R80(mm)	FWHM$_{\mathrm{MC}}$(mm)	FWHM$_{\mathrm{mR}}$(mm)	Δ FWHM(mm)
73,4	44,1	45,0	0,9	4,1	4,0	0,1
76,1	47,3	48,1	0,8	4,6	3,8	0,7
78,7	50,1	50,6	0,5	4,6	4,4	0,2
81,4	53,2	54,2	1,0	5,0	4,2	0,8
83,8	56,5	57,1	0,6	5,3	4,8	0,5
86,3	59,1	59,6	0,4	5,4	4,5	0,9
88,7	62,6	63,3	0,7	5,8	5,1	0,7
91,0	65,6	66,3	0,7	6,0	4,9	1,1
93,4	68,2	69,2	1,0	6,2	5,4	0,8
95,6	71,7	71,8	0,1	6,5	5,9	0,6
97,8	74,1	74,6	0,5	6,8	5,7	1,1
100,0	77,2	77,8	0,6	7,0	6,1	0,9
102,1	80,3	80,5	0,2	7,2	6,6	0,6
104,2	83,4	83,6	0,3	7,5	7,3	0,2
106,3	86,3	87,0	0,7	7,8	6,9	0,9
108,4	89,2	90,1	0,9	8,1	7,6	0,5
110,4	92,0	92,5	0,5	8,2	7,3	0,9
112,4	95,3	95,9	0,6	8,6	6,9	1,7
114,4	98,5	99,1	0,7	8,8	8,2	0,6
116,4	101,5	101,8	0,3	9,0	8,1	0,9
118,3	104,4	104,5	0,1	9,3	8,6	0,7
120,2	107,3	107,7	0,4	9,6	9,2	0,4
122,0	110,5	110,4	0,1	9,9	8,7	1,2
123,9	113,4	113,4	0,0	10,0	9,3	0,7
125,7	116,1	116,8	0,7	10,2	9,0	1,2
127,5	119,2	119,5	0,3	10,5	9,5	1,0
129,4	122,6	122,7	0,0	10,9	10,4	0,5
131,2	125,3	125,4	0,1	11,0	9,9	1,1
132,9	128,3	128,9	0,6	11,3	10,5	0,8
134,7	131,3	131,1	0,2	11,5	11,1	0,4
136,4	134,4	134,1	0,3	11,7	10,8	0,9
138,1	137,3	137,7	0,3	12,0	11,4	0,6
139,9	140,1	140,7	0,5	12,2	10,4	1,8
141,5	143,2	143,0	0,2	12,5	11,6	0,8
143,2	146,3	146,4	0,1	12,8	11,5	1,3
144,9	149,1	149,1	0,0	13,0	11,2	1,8
146,5	152,1	152,4	0,3	13,1	12,6	0,6
148,2	155,1	155,7	0,7	13,5	12,2	1,3
149,8	158,1	158,4	0,3	13,7	12,2	1,5
151,4	161,1	161,4	0,3	14,0	12,8	1,3
153,0	164,1	164,1	0,0	14,3	12,4	1,9
154,6	167,0	167,5	0,5	14,5	14,1	0,4
156,2	169,9	170,3	0,4	14,7	13,7	1,0
157,8	172,8	173,4	0,6	14,9	13,7	1,2
159,3	176,0	175,9	0,1	15,3	14,4	0,9
160,8	179,0	179,3	0,4	15,4	14,1	1,3
162,4	181,8	182,2	0,4	15,7	14,6	1,1
163,9	184,9	185,2	0,3	15,9	15,1	0,9
165,5	187,8	188,5	0,7	16,2	14,5	1,7
167,0	190,8	191,5	0,7	16,5	15,0	1,5
168,5	193,7	193,9	0,2	16,8	15,7	1,1
169,9	196,7	197,0	0,4	16,9	15,8	1,1
171,4	199,7	200,2	0,5	17,2	16,3	0,9
172,9	202,5	203,2	0,7	17,4	16,2	1,2
174,4	205,8	205,9	0,1	17,8	16,8	1,0
175,8	208,5	208,8	0,3	17,9	16,5	1,5
177,3	211,6	212,1	0,5	18,1	17,2	0,9
178,7	214,5	215,0	0,5	18,4	17,1	1,2
180,2	217,3	217,6	0,3	18,6	17,3	1,3
181,6	220,5	221,4	0,9	19,0	17,5	1,4
183,0	223,4	223,9	0,5	19,2	17,7	1,5
184,4	226,7	227,2	0,5	19,6	19,0	0,6
185,8	229,4	229,8	0,4	19,6	18,8	0,8
187,2	232,5	232,6	0,1	19,9	18,6	1,3
188,6	235,3	235,4	0,1	20,5	19,5	1,0
190,0	238,2	238,5	0,3	20,5	19,9	0,6
191,4	241,5	241,8	0,3	20,8	19,8	1,0
192,8	244,4	244,8	0,4	21,0	19,6	1,4
194,1	247,3	247,4	0,0	21,2	19,8	1,4
195,4	250,4	250,5	0,1	21,6	20,6	0,9
196,8	253,2	254,1	0,9	21,7	21,0	0,7
198,2	256,2	256,5	0,3	22,0	20,3	1,7
199,5	259,2	260,0	0,8	22,2	21,9	0,3
200,8	262,4	262,7	0,3	22,8	22,1	0,6
202,2	265,3	265,7	0,3	22,6	21,9	0,7
203,5	268,5	268,7	0,2	22,9	21,6	1,3
204,8	271,3	271,5	0,2	23,3	21,7	1,6
206,1	274,3	274,9	0,7	23,5	22,4	1,1
207,4	277,1	277,6	0,6	23,8	23,3	0,5
208,7	280,0	280,6	0,5	24,0	23,6	0,5
210,0	282,9	283,5	0,6	24,3	23,5	0,8
211,3	286,2	286,7	0,5	24,7	23,2	1,5
212,6	289,0	289,6	0,6	24,6	24,1	0,6
213,9	292,0	292,2	0,2	25,0	24,2	0,8
215,2	295,0	295,9	0,9	25,2	24,2	1,1
216,4	298,2	298,8	0,7	25,6	24,6	1,0
Average			0,4			1,0

Table 4.1: Ranges and Full Width at Half Maximums (FWHM) of all 86 beams in the machine used in matRad and their corresponding simulated beam in TOPAS. The undertexts $_{MC}$ and $_{mR}$ refer to TOPAS Monte Carlo simulations and matRad values, accordingly.

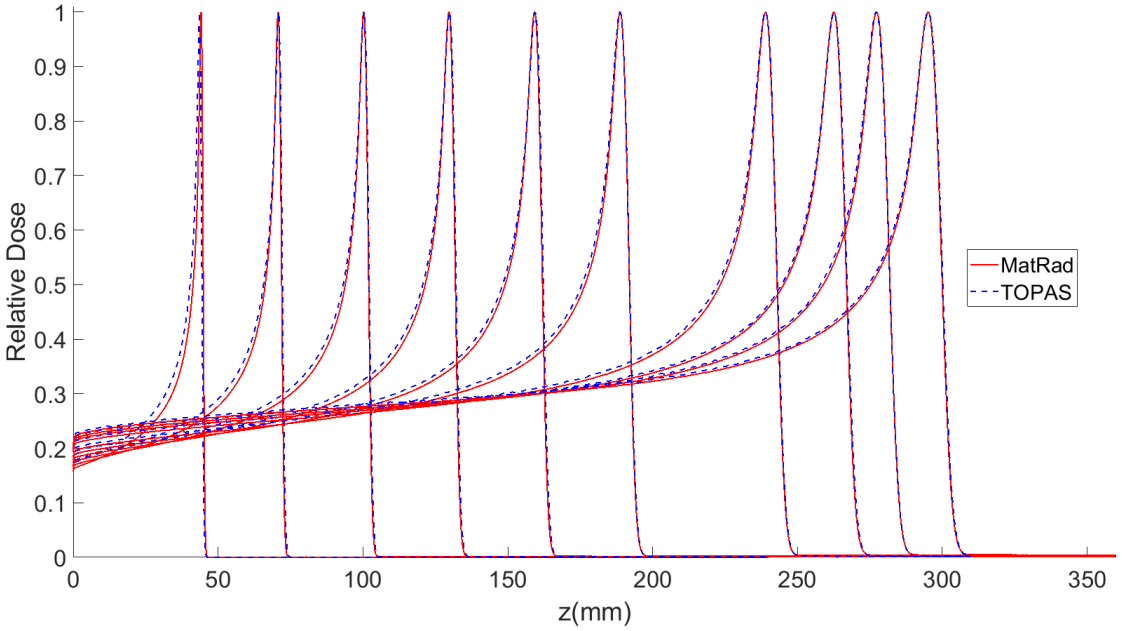

Figure 4.4: Comparison of depth dose distributions between MatRad beams of 73.41 MeV, 95.59 MeV, 116.36 MeV, 134.68 MeV, 151.44 MeV, 166.98 MeV, 191.38 MeV, 202.16 MeV, 208.72 MeV and 216.45 MeV, from left to right, and the corresponding beams simulated with TOPAS. Each beam is normalized to its maximum.

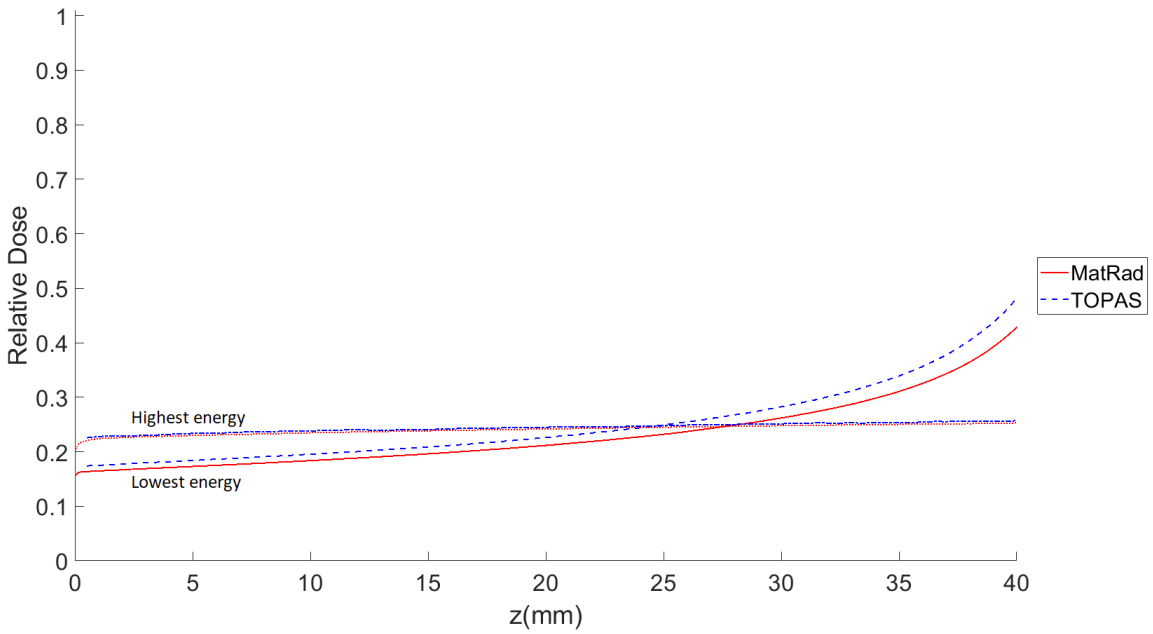

Figure 4.5: Focus on the entry dose. The difference is more noticeable for smaller energies while for larger ones it's almost non-existent

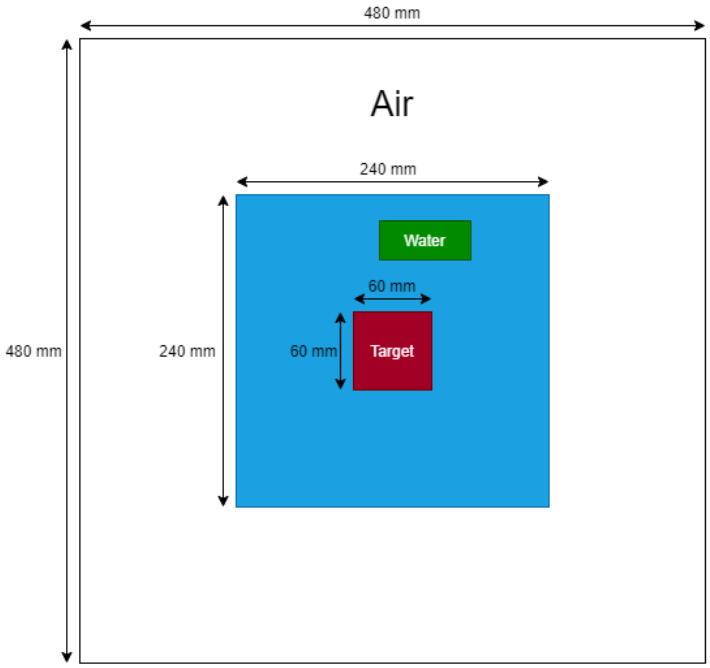

Figure 4.6: Geometry of the phantom for the box phantom simulations.

water, which corresponds to the volume where dose was scored in the TOPAS simulation. The target region where the dose is supposed to be constant is a smaller 60x60x60 mm^3 cube placed in the middle of the 240mm side cube. Having imported the data, both the RTct and RTsegmentation variables are automatically defined, using the graphical user interface (GUI), the RTplan variable is easily created by choosing the radiation mode and corresponding machine, in this case the machine which was validated in section (4.2), as well as the constraints and objectives, that can be seen in Table 4.2, bixel width, gantry and couch angles, and finally scan spots locations which can be seen in Figure 4.7. With the information from RTct, RTsegmentation and RTplan matRad can now generate the RTdij and RTarran-jarnome variables and then taking into account all five variables matRad optimizes the weights for each beam and scan spot by minimizing the difference between objective and delivered dose to the ROI and generates the RTresult variable.

The next step is extracting the necessary information from matRad to be able to setup the required parameter files for the TOPAS simulations. The relevant parameters to be extracted are the energies of the used beams, the scan spots and weights for each beam and spot since others such as the size of the phantom or bin size are defined previously. These parameters are obtained and written into text files using a personalized script developed in MATLAB. Here is where TOPAS hierarchy control shows its advantages, knowing which beams are used, and having previously defined parameter files for each of the 86 beams in the matRad machine, the information of each beam is included in the simulation through one of TOPAS features. The ability to handle time varying parameters is also very helpful in this situation, there are 169 scan spots. Without time features 169 simulations would be needed, one for each scan spot and then the data would have to be combined, with time features the position of the source and weight of the beam can be changed to cover all 169 spots with each beam in a single simulation eliminating the need for further treatment of the data.

The resulting dose for the simulation can be seen in Figure 4.8. The dose is normalized since there was no strict objective on how much dose should be delivered to the target, only dose to target in relation to dose to surrounding areas. This allowed simulations to be ran with only the number of histories necessary to achieve statistically relevant results and a smooth dose distribution instead of

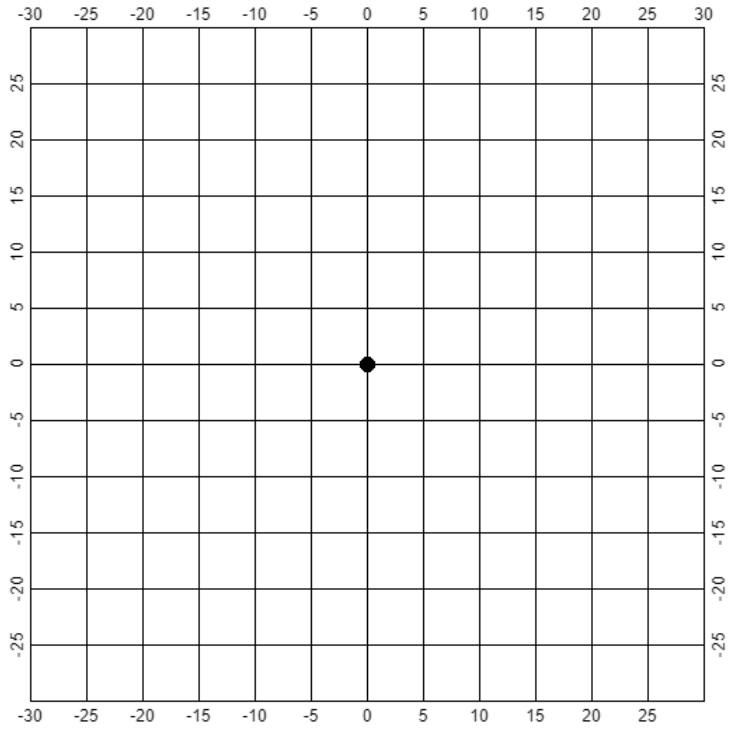

Figure 4.7: Chosen scan spots for the target on the right, the values are in mm and are relative to the isocenter of the phantom.

VOI	Priority	Optimization	Function	Penalty	Par 1	Par 2	Type
Organ at Risk	2	Objective	Squared overdosing	100	Dose=$\frac{1}{12}$		Predefined
Target	1	Objective	Squared deviation	800	Dose=1		Predefined
Target	1	Constraint	Minimum DVH	800	Dose=1	Vol=0.95	User

Table 4.2: Objectives and constraints for the optimization of dose to the box phantom simulation. DVH stands for Dose Volume Histogram.

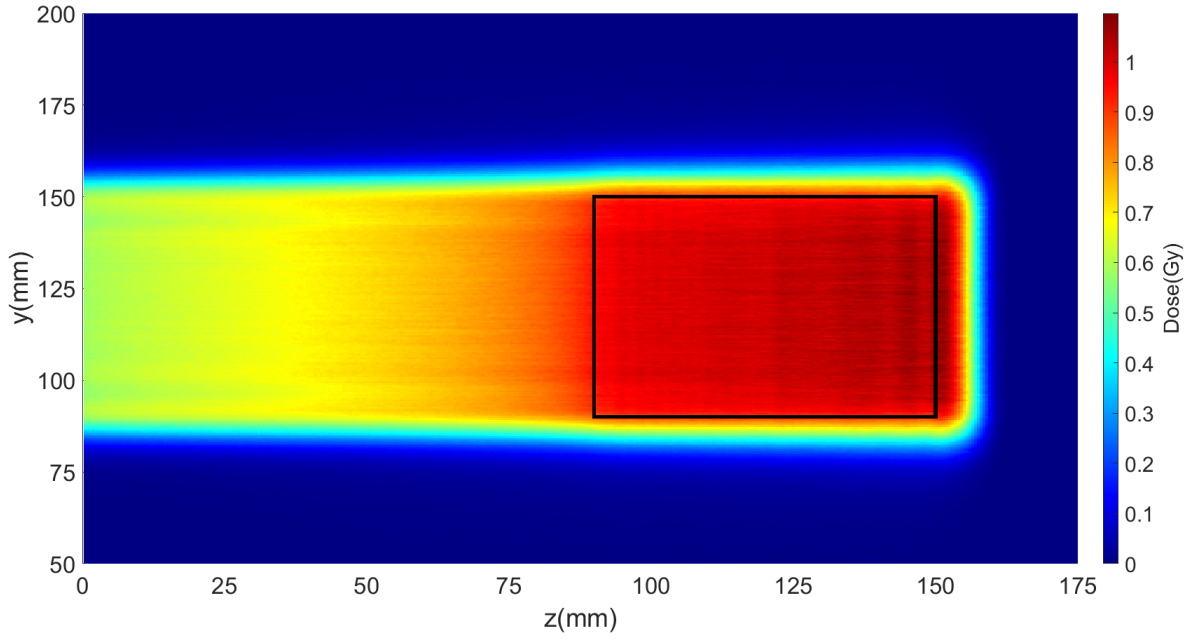

Figure 4.8: Dose delivered to the phantom in the box phantom plan. The black contour marks the target.

Material	R_{80}(mm)	Coverage(%)
Water	154.3	93.4
Water-like muscle	155.6	92.5
Water-like adipose tissue	153.8	94.3

Table 4.3: Range and coverage for both the water and water-like materials phantoms plans.

enough particles to achieve a certain dosage, like it would have to be done for an actual plan with a specific Gy dose objective. Taking this into account, a satisfactory result was achieved, 93.4% of the target received at least 0.95 of the maximum dose and the dose had a range of 154.3 mm, 4.3 mm more than the target, therefore tissues located downstream of the target would be spared.

4.4 Errors due to misassignments

The goal of this chapter is verifying the impact of missassigment errors of the CT on the final dose. The impact of these missassignments will be quantified in the worst case scenario, a case where all voxels in a phantom had such errors.

The base phantom is the same as in section (4.3), a cube entirely made of water. The two test phantoms are cubes of the same dimensions as the previous but with a material that has the same density and mean excitation energy as water but with the composition of muscle, in one case, and adipose on the other. The composition for both water-like muscle and water-like adipose tissue are the same as in Table 3.1 from section (3.2).

The setup for the simulations is also the same as in section (4.3) and can be seen in Figure 4.6, the simulations for the water-like muscle and water-like adipose tissue are ran with the weights for each beam and scan spot calculated in section (4.3) as if the phantom was composed of water, this allows the assessment of the cumulative impact of material missassignment errors on the dose delivered to the phantom, if the cumulative error in this worst case scenario setup is not significant then it can be stated with confidence that sporadic errors will have a very small or negligible impact on the final dose.

The dose distribution for the water-like muscle and water-like adipose tissue simulations are presented in Figure 4.9 and Figure 4.10, respectively, and the ranges and coverage are in Table 4.3, it can be observed that the differences in range are within the clinically accepted margins and the coverage is still above 92%. Based on this information it can be inferred that in this simple box phantom case errors in tissue assignment are not relevant to the final dose. It is important to mention that the coverage could be improved by continuing to tweak the constraints on the dose to achieve a more optimized dose delivery, of course this process would be extremely time consuming especially taking into account that the computer used at the time only had 4 threads, because of this the decision to accept this greater than 92% coverage was made due to time constraints.

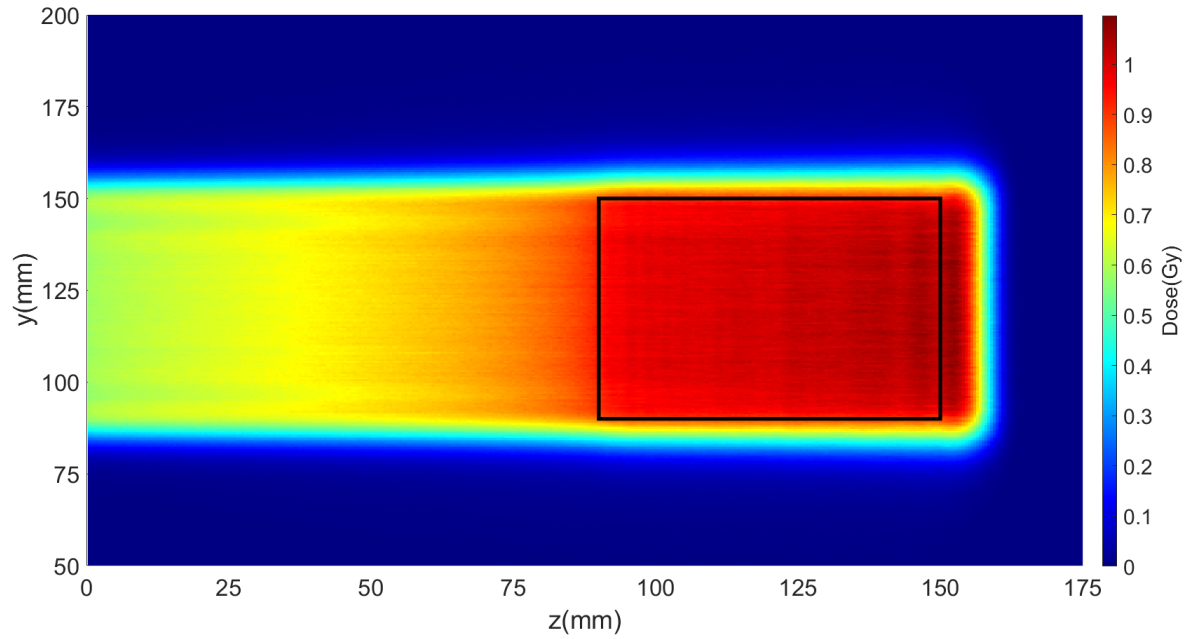

Figure 4.9: Dose delivered to the water-like muscle phantom. The black contour marks the target.

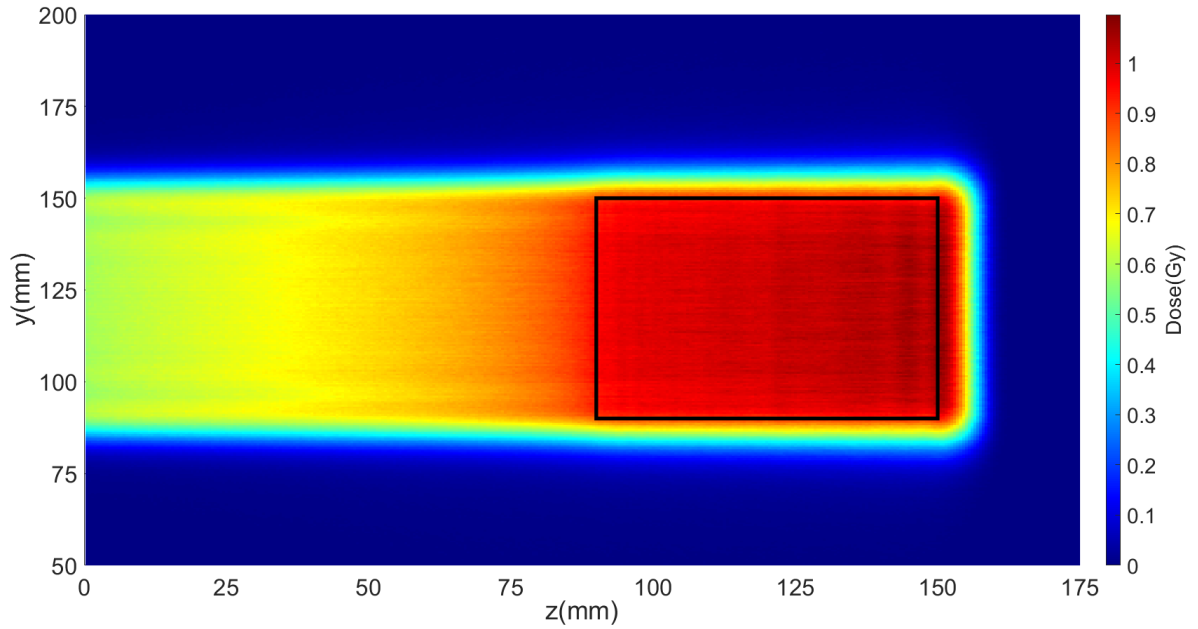

Figure 4.10: Dose delivered to the water-like adipose tissue phantom. The black contour marks the target.

Chapter 5

Treatment Plan

5.1 Motivation

Before starting this chapter, a remark should be made regarding computational power. The computer used throughout this work was upgraded from an older generation 4Gb RAM with 4 threads laptop to a 32Gb RAM with 16 threads desktop. This upgrade took place roughly when the work presented on this chapter started and it allowed for much powerful and faster calculations, that would not have possible with the previous set-up.

Following the successful validation of the MC beam model discussed in the previous chapter, a single beam proton treatment plan for a clinical case was created using matRad where the end goal is to once again assess the impact of composition missassignments in the patient CT on the delivered dose.

The treatment plan was developed for a brain tumour since head and neck cancers are the seventh most common type of cancer having 888 thousand estimated new cases in 2018 and causing 453 thousand deaths [17], also for the purpose of this work a smaller tumor was preferable instead of the even more common *medulloblastoma* due to computational time constraints.

5.2 Development

5.2.1 Setup

The CT of an oncological patient with the structures already delineated by specialists was used. The first step to develop the treatment plan is analogous to section (4.3), the CT data is imported to matRad, which in turn generates the RTct and RTsegmentation variables. In the Box Phantom case, the parameters for the plan were simple, as the phantom was homogeneous (rotations of the couch and gantry were redundant), this is not the case in this section and therefore the angles must be chosen, correctly, to minimize the dose delivered to organs at risk shown in Figure 5.1. The proton treatment plan shared by the provider of the patient data together with the CT used 3 different gantry and couch angles to achieve an uniform dose in the tumour, while minimizing damage to adjacent healthy tissues, the most prominent (having more impact on total dose) being gantry and couch angles of 300^{o} and 90^{o}, respectively. In this work, the goal is not to necessarily simulate the most optimized treatment plan, but rather evaluating the effects of density missassignments in the CT. Using three different configurations would not only greatly increase the computation time of the simulations but more importantly bring difficulties to the evaluation of the impact of the missassignments errors as the most important parameter to quantify these will be the range of the dose. The combination of three beams could hide these effects and would make the

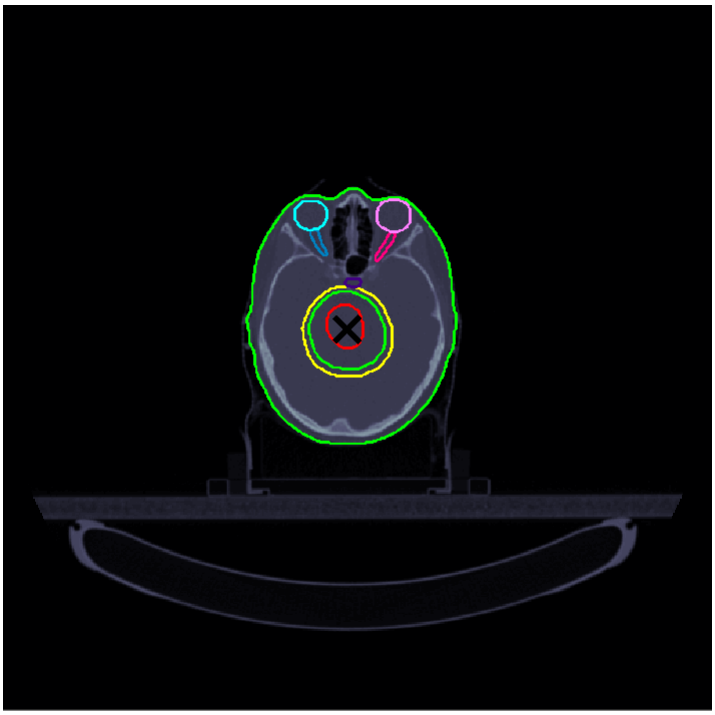

Figure 5.1: Axial view of the CT at the isocenter with delineated organs at risk and targets, GTV in red, CTV in green, PTV in yellow, left and right eye in pink and blue respectively, left and right optical nerves in dark pink and dark blue respectively and pituitary gland in purple.

VOI	Priority	Optimization	Function	Penalty	Par 1	Type
PTV	1	Objective	Squared deviation	800	Dose=1	Predefined
GTV	1	Objective	Squared deviation	800	Dose=1	Predefined
CTV	1	Objective	Squared deviation	800	Dose=1	Predefined

Table 5.1: Objectives and constraints for the optimization of the treatment plan.

definition of R80 very complex for each beam. For this reason, a single beam configuration was used. This configuration still has to be able to deliver a conformal dose to the tumour while avoiding organs at risk since the results will be more relevant if acquired from a setup which could be used in a clinical setting.

A combination of a gantry angle of 270^{o} and a couch angle of 90^{o}, similarly to the 300^{o} and 90^{o} used in the provided plan, has the particle beams enter the body through the back of the head and avoids delivering dose to the eyes when optimized, which is shown in Figure 5.2. A set of constraints regarding the target were already provided alongside the CT and can be seen in Table 5.1. Due to lack of data and clinical expertise, no constrains were set to the OARs, as it would be expected clinically.

The parameters optimized in matRad were then extracted into text files to be used in TOPAS, this was done through a personalized MATLAB script similar to the one used in section (4.3) (more complex as would be expected).

5.2.2 HU to material Conversion

One file in particular is of extreme relevance to this work since it is what will allow the introduction and posterior assessment of errors in tissue assignment. In the Box Phantom case the phantom was created directly in TOPAS by defining its half lengths in the three dimensions and its material, in this section the Hounsfield Units in the CT must be converted into material densities and compositions for each voxel.

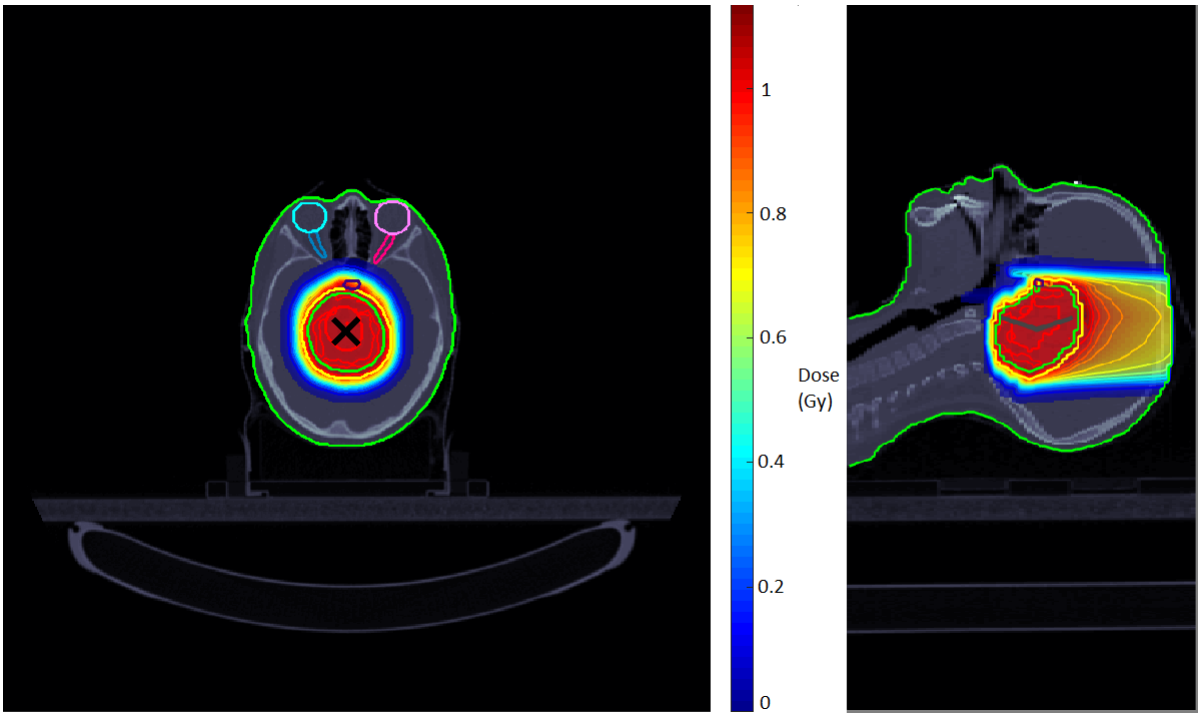

Figure 5.2: Axial (left) and sagital (right) views of the CT with the dose delivered through matRad optimization. No dose is delivered to either eye or optical nerve.

The used method follows the work of [18] which details how HU units can be converted into mass density and composition.

The goal of this section is to achieve a relation between HU (defined in section (2.12) and the density and composition of each material.

[19] demonstrates that most skeletal tissues are composed of only osseous tissue and bone marrow, barring a few exceptions that contain cartilage. This allows for the skeletal tissues to be represented by their proportions of bone marrow and osseous tissue, the density can then be interpolated in the range that covers skeletal tissues.

The parameters that describe each material are (ρ_1, $w_{1,i}$,H1) and (ρ_2, $w_{2,i}$,H2), ρ where ρ_1 and ρ_2 represent the density of bone marrow and cortical bone, respectively, $w_{1,i}$ and $w_{2,i}$ represent the elemental weights in bone marrow and cortical bone respectively and H1 and H2 represent the Hounsfield units of bone marrow and cortical bone, respectively. We can write the following equations:

$$w_i = W_1 \times w_{1,i} + W_2 \times w2, i = W_1(w_{1,i} - w2, i) + w_{2,i} \tag{5.1}$$

where W_1 and W_2 represent the percentages of bone marrow and cortical bone, respectively and W_2=1-W_1.

$$\rho = \frac{m}{V} = \frac{m}{\frac{m_1}{\rho_1} + \frac{m_2}{\rho_2}} = \frac{1}{\frac{W_1}{\rho_1} + \frac{1-W_1}{\rho_2}} = \frac{\rho_1\rho_2}{W_1(\rho_2 - \rho_1) + \rho_1} \tag{5.2}$$

Substituting equation 5.1 and equation 5.2 into equation 2.4 the attenuation coefficient can be expressed as:

$$\begin{aligned} \mu &= \frac{\rho_1\rho_2}{W_1(\rho_2 - \rho_1) + \rho_1} \times N_A \times [W_1 \times (\sum_i \frac{w_{1,i} - w_{2,i}}{A_i} \times \sigma_i) + \sum_i \frac{w_{2,i}}{A_i} \times \sigma_i] \\ &= \frac{\rho_1\rho_2}{W_1(\rho_2 - \rho_1)}[W1 \times (\frac{\mu_1}{\rho_1} - \frac{\mu_2}{\rho_2}) + \frac{\mu_2}{\rho_2}] \end{aligned} \tag{5.3}$$

			Elemental weights (%)						
Tissue	**HU**	**ρ(g cm^{-3})**	**H**	**C**	**N**	**O**	**P**	**Ca**	**Others**
adipose 3	-98	0.93	11.6	68.1	0.2	19.8	0	0	0.3
Bone marrow	-22	1.00	11.0	52.9	2.1	33.5	0.1	0	0.4
Adrenal gland	14	1.03	10.6	28.4	2.6	57.8	0.1	0	0.5
Small intestine	23	1.03	10.6	11.5	2.2	75.1	0.1	0	0.5
Skin 3	77	1.09	10.1	15.8	3.7	69.5	0.1	0	0.8
Connective tissue	100	1.12	9.4	20.7	6.2	62.2	0	0	1.5
Cortical Bone	1524	1.92	3.4	15.5	4.2	43.5	10.3	22.5	0.6

Table 5.2: HU, densities and compositions of the materials used for interpolation with equation 5.6. Adapted from [18].

and combining with equation 2.5

$$W_1 = \frac{\rho_1(H_2 - H)}{(\rho_1 H_2 - \rho_2 H_1) + (\rho_2 - \rho_1)H} \tag{5.4}$$

Finally by replacing equation 5.4 in equation 5.1

$$w_i = \frac{\rho_1(H_2 - H)}{(\rho_1 H_2 - \rho_2 H_1) + (\rho_2 - \rho_1)H} \times (w_{1,i} - w2, i) + w_{2,i} \tag{5.5}$$

and in equation 5.2

$$\rho = \frac{\rho_1 H_2 - \rho_2 H_1 + (\rho_2 - \rho_1)H}{H_2 - H_1} = \text{Offset} + \text{Factor} \times H \tag{5.6}$$

where Offset=$\frac{\rho_1 H_2 - \rho_2 H_1}{H_2 - H_1}$ and Factor=$\frac{\rho_2 - \rho_1}{H_2 - H_1}$.

Equations 5.5 and 5.6 are valid in the region $H_1 \leq H \leq H_2$ and give direct functions between HU and density and elemental weights for skeletal tissues.

Soft tissues are composed of water, fat and protein therefore the functions derived above are not directly applicable to them yet by applying them for fat and water it has been shown that densities are calculated with 0.01 g cm^{-3} or more accuracy [18]. TOPAS uses a slightly different formula for density as it needs to be applicable to the full range of HUs.

$$\rho_{\text{TOPAS}} = [\text{Offset} + (\text{Factor} \times (\text{FactorOffset} + H)] \times \text{DensityCorrection} \tag{5.7}$$

where FactorOffset is used for the sections where the densities are lineraly interpolated and DensityCorrection takes into account the differences between TOPAS and the used Treatment Planning System. There are 7 different sections where the formula is applied. From -1000HU to -98 HU the mass densities of air and adipose 3 are interpolated, 1.21$\times 10^{-3}$ g cm^{-3} and 0.93 g cm^{-3},respectively, from -98HU to 14HU equation 5.6 is used for adipose 3 and adrenal gland, from 14HU to 23HU the density is set to 1.03 g cm^{-3}, from 23HU to 100HU equation 5.6 is used for small intestine and connective tissue, from 101 to 2000 equation 5.6 is used for bone marrow and cortical bone, this is the range of skeletal tissues, from 2001 to 2994 the densities of cortical bone and titanium are interpolated and finally 2995HU is set to the density of titanium as it is meant to take into account possible implants in the patient. The HU values and compositions of the relevant materials can be seen in Table 5.2 and the functions for each interval in Table 5.3.

While the densities are a continuous function, the compositions must be assigned beforehand and divided into bins, TOPAS once again closely follows of the work of Schneider et al [18]. There are 25 bins which can be seen in Table 5.4, the difference here is that the bin assigned to cortical bone is extended until 2995HU and there is an additional bin with the composition of titanium. With both a continuous

HU	Offset	Factor	FactorOffset
-1000 – -99	0.00121	0.001029700665188	1000
-98 – 14	1.018	0.000893	0
15 – 22	1.030	0	1000
23 – 100	1.003	0.001169	0
101 – 2000	1.017	0.000592	0
2001 – 2994	2.201	0.0005	2000
2995 – 2996	4.540	0	0

Table 5.3: Parameters in equation 5.7 for each of the 7 HU sections.

HU	H	C	N	O	Mg	P	S	Cl	Ar	Ca	Na	K	Ti	
-1000 – -950	0	0	75.5	23.2	0	0	0	0	1.3	0	0	0	0	air
-950 – -120	10.3	10.5	3.1	74.9	0	0.2	0.3	0	0	0.2	0.2	0.2	0	lung
-120 – -83	11.6	68.1	0.2	19.8	0.0	0.0	0.1	0.1	0	0	0.1	0	0	*
-82 – -53	11.3	56.7	0.9	30.8	0	0	0.1	0.1	0	0	0.1	0	0	*
-52 – -23	11.0	45.8	1.5	41.1	0	0.1	0.2	0.2	0	0	0.1	0	0	*
-22 – 7	10.8	35.6	2.2	50.9	0	0.1	0.2	0.2	0	0	0	0	0	*
8 – 18	10.6	28.4	2.6	57.8	0	0.1	0.2	0.2	0	0	0	0.1	0	*
18 – 80	10.3	13.4	3.0	72.3	0	0.2	0.2	0.2	0	0	0.2	0.2	0	**
80 – 120	9.4	20.7	6.2	62.2	0	0	0.6	0.3	0	0	0.6	0	0	connective tissue
120 – 200	9.5	45.5	2.5	35.5	0	2.1	0.1	0.1	0	4.5	0.1	0.1	0	*
200 – 300	8.9	42.3	2.7	36.3	0	3.0	0.1	0.1	0	6.4	0.1	0.1	0	*
300 – 400	8.2	39.1	2.9	37.2	0	3.9	0.1	0.1	0	8.3	0.1	0.1	0	*
400 – 500	7.6	36.1	3.0	38.0	0.1	4.7	0.2	0.1	0	10.1	0.1	0	0	*
500 – 600	7.1	33.5	3.2	38.7	0.1	5.4	0.2	0	0	11.7	0.1	0	0	*
600 – 700	6.6	31.0	3.3	39.4	0.1	6.1	0.2	0	0	13.2	0.1	0	0	*
700 – 800	6.1	28.7	3.5	40.0	0.1	6.7	0.2	0	0	14.6	0.1	0	0	*
800 – 900	5.6	26.5	3.6	40.5	0.2	7.3	0.3	0	0	15.9	0.1	0	0	*
900 – 1000	5.2	24.6	3.7	41.1	0.2	7.8	0.3	0	0	17.0	0.1	0	0	*
1000 – 1100	4.9	22.7	3.8	41.6	0.2	8.3	0.3	0	0	18.1	0.1	0	0	*
1100 – 1200	4.5	21.0	3.9	42.0	0.2	8.8	0.3	0	0	19.2	0.1	0	0	*
1200 – 1300	4.2	19.4	4.0	42.5	0.2	9.2	0.3	0	0	20.1	0.1	0	0	*
1300 – 1400	3.9	17.9	4.1	42.9	0.2	9.6	0.3	0	0	21.0	0.1	0	0	*
1400 – 1500	3.6	16.5	4.2	43.2	0.2	10.0	0.3	0	0	21.9	0.1	0	0	*
1500 – 2995	3.4	15.5	4.2	43.5	0.2	10.3	0.3	0	0	22.5	0.1	0	0	*
2995 – 2996	0	0	0	0	0	0	0	0	0	0	0	0	100	titanium

Table 5.4: Elemental weights in percentage for each bin of Hounsfield Units. Bins marked with * in the final column were interpolated using equation 5.5 within their corresponding values, the bin marked with $*_*$ has the mean values of every tissue with HU number in the interval, every other bin has the composition of the stated material.

function for densities and the division into bins for composition Hounsfield Units in the CT can now be converted into material properties for each voxel and the simulation can be ran. A TOPAS parameter file for the treatment plan is discussed in Appendix(A).

5.3 Errors due to misassignments

In all the previous chapters, the missassignments were introduced by simply changing the material of the phantoms, whereas that was not possible here since changing the entirety of the CT for these materials would not be realistic. Therefore the errors will be introduced by changing only the voxels in which either adipose or muscle are located. Changing the HU numbers directly on the CT would be hard since it would require previous knowledge of all the HUs in the CT. The more efficient solution is changing the way in which the HUs are transformed into densities and compositions, once again water-like muscle and water-like adipose tissue materials will be the introduced errors. This was done by having all voxels, which would be composed of muscle or adipose, maintaining their respective compositions, as seen in Table 3.1, but being assigned the density of water. Looking back at equation 5.7, which transforms

HUs into densities, the final term (Density Correction) is used to account for the differences between TOPAS and the used Treatment Planning System (TPS). This is the factor which allows the introduction of errors, in this work no specific TPS is used so the corrective term would be set to 1 for all HUs, to introduce the errors the corrective term is set in a way that forces the density of HUs corresponding to muscle or adipose to be that of water (1 g cm^{-3}). This is done through a personalized MATLAB script which calculates the density assigned to each HU and then the necessary correction which is afterwards converted into a parameter in the correct form needed to be introduced into TOPAS. The correction is applied from -98 HU (adipose 3) and 77 HU (Skin 3) which set the boundaries for adipose on the low end and muscle on the top end (Table 5.2).

5.4 Results

The dose delivered to both the unaltered HU conversion and corrected HU conversion to introduce errors can be seen in 3 different views, an axial view in , a sagital view in and a coronal view, all shown in Figure 5.3. The differences in range are very subtle and nigh impossible to see in these different views. In order to calculate the differences in range due to missassignments in the CT, the sagital plane was chosen as it provedes the better of the dose. The calculations are made in the Beam Eye View (BEV, section (2.9)) and calculate for all relevant X and Y around the isocenter the range of dose for that specific straight line of voxels, this is where the decision to have the beams placed at 270º instead of 300º comes into fruition as if the beam was oblique it would greatly complicate the calculations.

In these calculations, the differences in range in the boundaries were neglected. The boundaries are associated with a high degree of uncertainty and the values there are may not be representative of the errors induced by missassignments in the CT. The ranges for each XY pair around the isocenter are depicted in Figure 5.4 and the difference between ranges for the simulations without and with introduction of errors can be seen in Figure 5.5. The average difference for the ranges defined as $R80_{\mathrm{corrected}}$-R80 is 3.5 mm with a standard deviation of 0.4 mm, 96.8% of the voxels had a difference greater than 0, the fact that the differences in range have, in large majority, the same sign is a good sign that the changes in the HU conversion method were correctly introduced since the differences are consistent.

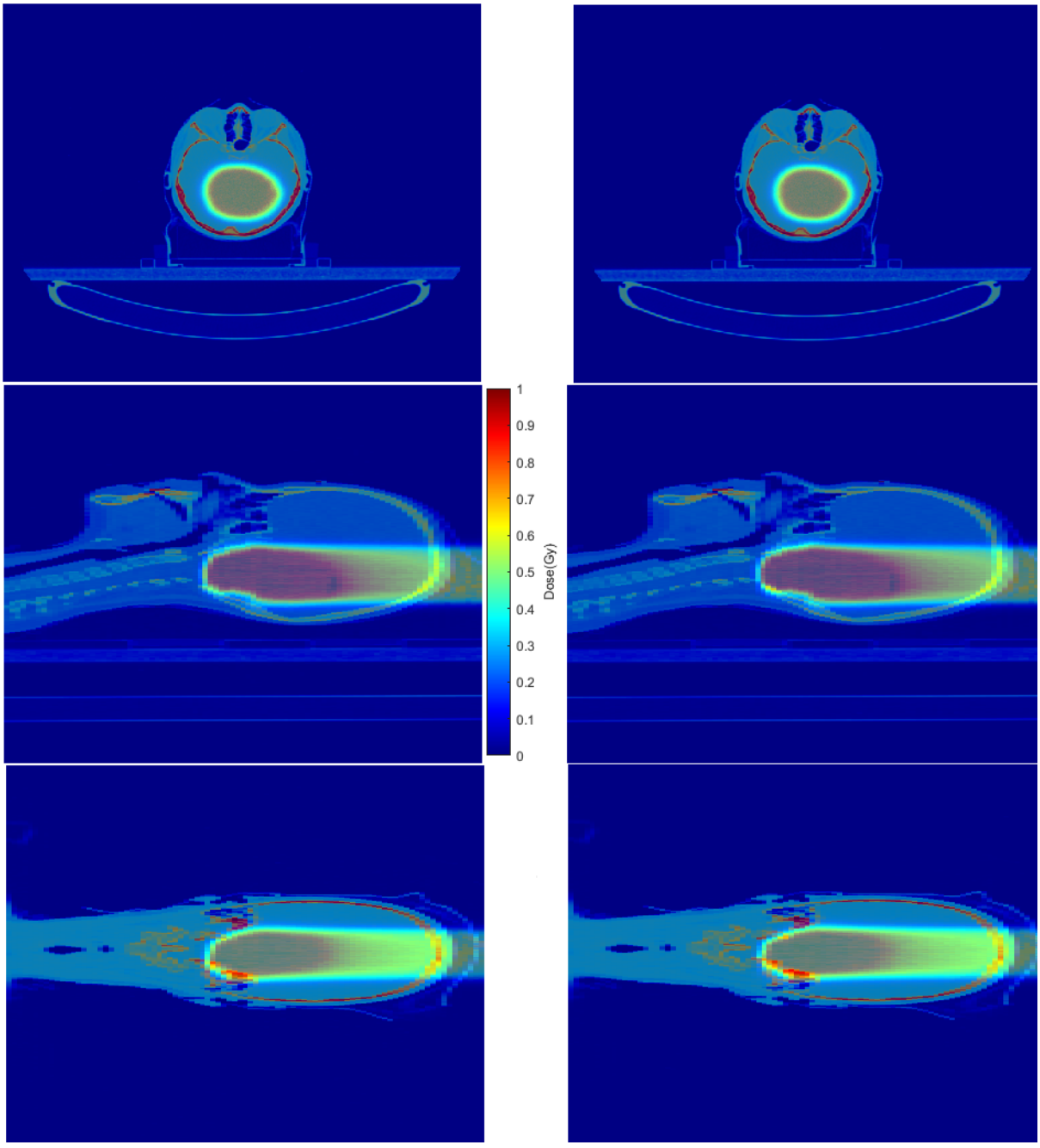

Figure 5.3: Comparison of the dose delivered to the patient seen from the axial plane on top, sagital plane on the middle and coronal plane on the bottom. Simulations without correction on the left and simulations with the correction on density to introduce missassignments on the right.

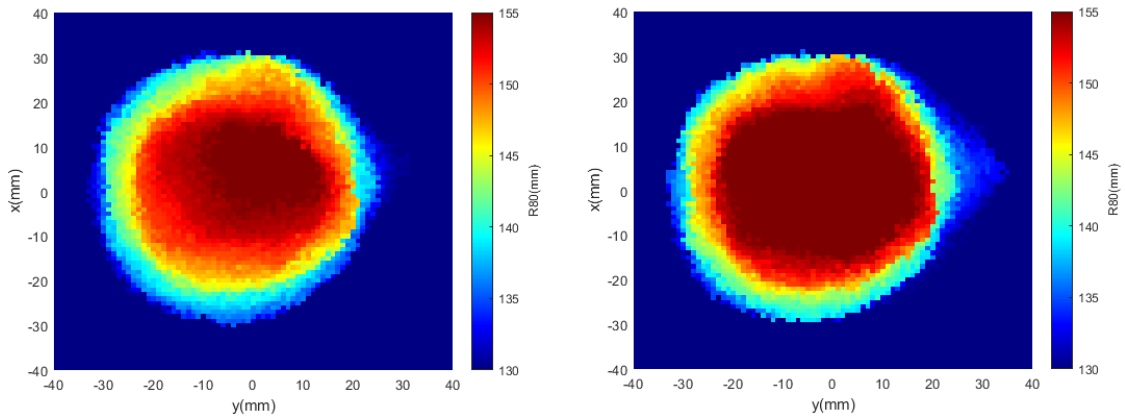

Figure 5.4: R_{80} for each X and Y, in the Beam Eye View, pair voxels for the simulation without introduction of errors on the left and the simulation with introduction of errors on the right. Distances are relative to the isocenter.

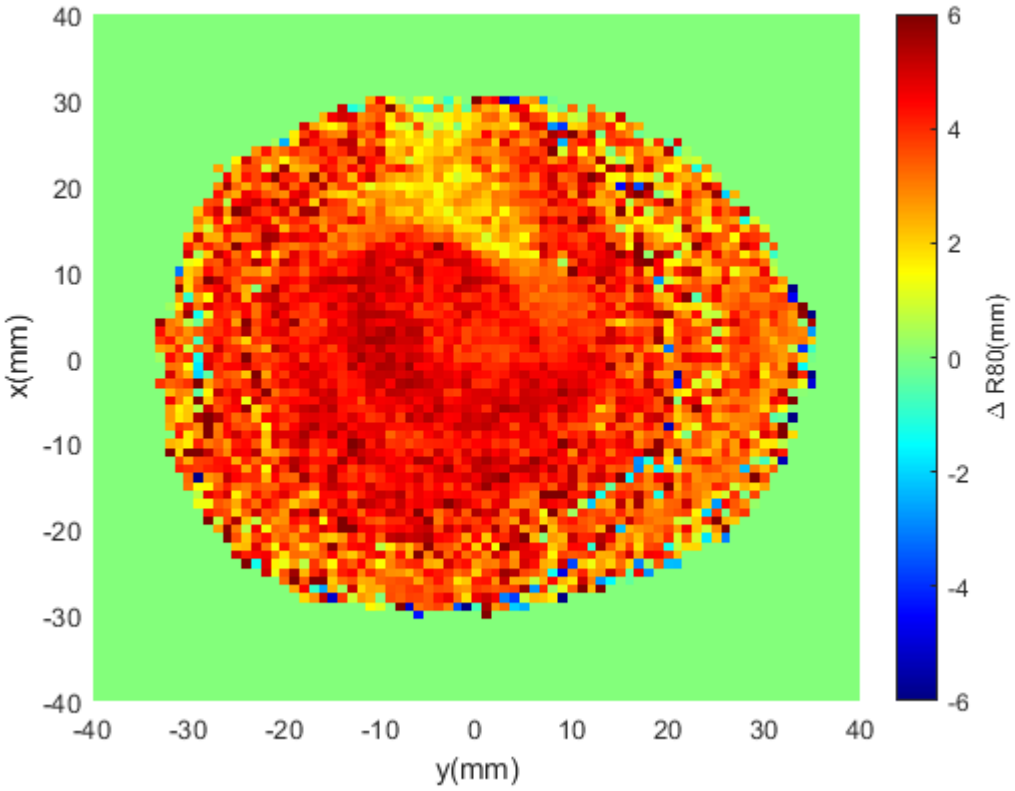

Figure 5.5: Differences in $_{80}$ for each X and Y, in the Beam Eye View, pair voxels between the simulation without introduction of errors and the simulation with introduction of errors. Distances are relative to the isocenter.

Chapter 6

Carbon Ions

6.1 Motivation

Particle beam radiotherapy can also be delivered using carbon ions. Interactions of ^{12}C ion beams with matter are similar to those of proton beams, the differences lie in the heavier mass of carbon ions and its higher charge as well. There are 2 main advantages ^{12}C ion beams have that make its study interesting. Firstly, their penumbra is sharper than in proton therapy, in proton beams the penumbra (section (2.10)) increases as the range increases while for carbon ions it remains almost constant as can be seen in Figure 6.1.

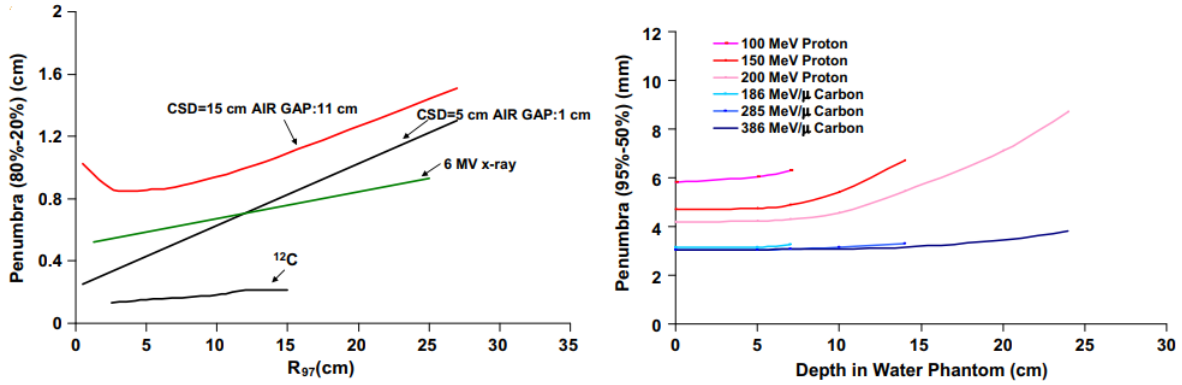

Figure 6.1: Comparison of penumbra for photon, proton and ^{12}C ion beams. Reproduced from [20].

The other advantage involves the Relative Biological Effectiveness (RBE, section (2.11)), for protons RBE can be approximated to 1.1 without significant errors [21], while for carbon ions it varies, RBE for ^{12}C ions increases until the Bragg Peak where it reaches its maximum and then decreases. This advantage comes from the fact than since RBE is at its highest at the Bragg Peak less physical dose will need to be delivered which eases the load on the patient while retaining the same biological damage to tumour cells. But this also brings a downside, since RBE varies the planning of the treatment can be significantly more complex, as this variation in RBE must be taken into account and the physical dose has to be adjusted to ensure an homogeneous dose covers the tumour, an example can be seen in Figure 6.2.

Another characteristic that must be taken into account is the fragmentation tail that appears in carbon ion beams, this happens because secondary particles are created during nuclear interactions with nucleus in the traversed medium, some of these secondary particles travel non negligible distances

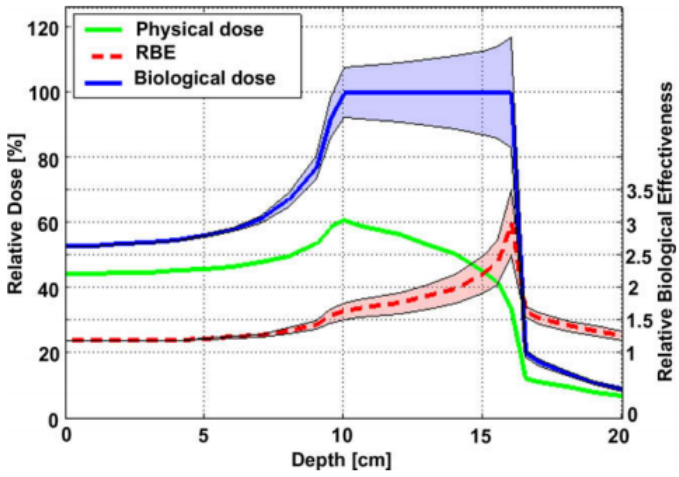

Figure 6.2: Variation of relative biological effectiveness (RBE) and consequent adjustments in given dose for a ^{12}C ion beam. Reproduced from [20].

beyond the range of the primary beam as can be seen in Figure 6.3.

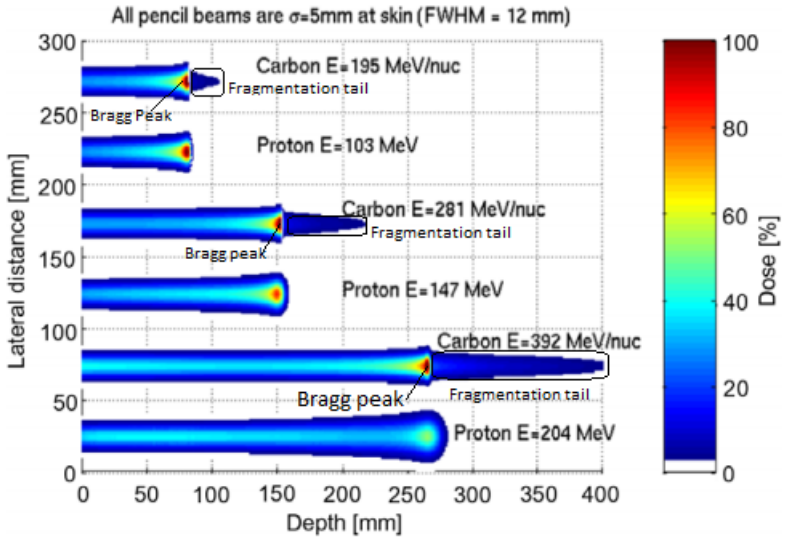

Figure 6.3: Comparison between the nonexistent fragmentation tail in proton beams versus the fragmentation tail, highlighted with a blue box, present in ^{12}C ion beams of different energies. Adapted from [20].

The main goal for this chapter was to once again study the impact of missassignment errors of the CT on the dose delivered to the patient.

6.2 Validation

As in section (4.2), the first step to be able to develop the treatment plan is to validate the beams in the chosen matRad machine, the setup is also the same as in that section.

Carbon ions having higher mass and higher atomic numbers interacts more strongly with the traversed medium, this, alongside with the formation of the fragmentation tail which forces particles to be

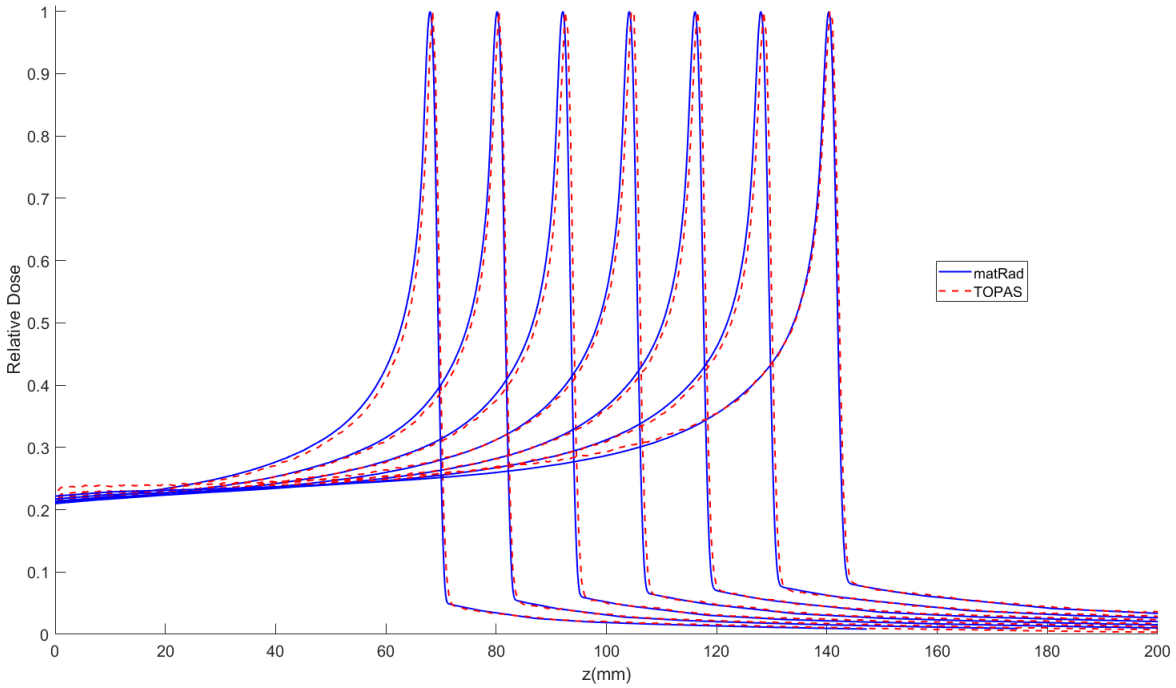

Figure 6.4: Comparison of depth dose distributions between matRad beams of 178.28 MeV/u, 195.18 MeV/u, 211.19 MeV/u, 226.46 MeV/u, 241.03 MeV/u, 255.17 MeV/u and 268.86 MeV/u, from left to right, and the corresponding beams simulated in TOPAS. Each beam is normalized to its maximum.

tracked for greater depths, causes the MC simulations for ^{12}C ion beams to be much more time consuming (about 50 times more time consuming for the same setup and number of histories), the process of validation for the proton beams was already the most time consuming section of the work so doing the same here would be impossible due to time constraints, even with the upgraded computer. To work around this issue, the box phantom chapter was skipped and the validation was performed only for the beams which would be used in the simulation of the treatment plan, which reduced the amount of validated beams from the 121 included in the machine to 21 used for the plan ranging from 178.28 MeV/u to 277.77 MeV/u and covering ranges from 68.9 mm to 149.8 mm.

Figure 6.4 shows that the TOPAS beams are at close accordance with the matRad beams, the figure also shows the very noticeable fragmentation tails in contrast to Figure 4.4 in which proton beams did not have dose after the Bragg Peak, it is also very noticeable that the FWHM of the carbon ion beams stays almost constant, varying from 6.0 mm to 7.5 mm while for protons of comparable range it varied from 6.2 mm to 13 mm.

Table 6.1 displays the values of FWHM and R80 for each energy as well as their corresponding absolute difference (Δ) when compared to the corresponding beam in the matRad machine and in the final row the average values of Δ.

Having an average Δ R80 of 0.2 mm and all values below 0.5 mm, which is the size of one voxel, corroborates the visual evidence seen in Figure 6.4 that the TOPAS beams have a identical behaviour to their corresponding beams in the matRad machine therefore the parameters calculated through matRad can be used to simulate treatment plans with TOPAS, in principle, without significant differences between the two.

Energy(MeV)	R80$_{\mathrm{MC}}$	R80$_{\mathrm{mR}}$(mm)	Δ R80(mm)	FWHM$_{\mathrm{MC}}$(mm)	FWHM$_{\mathrm{mR}}$(mm)	Δ FWHM(mm)
178.28	69.2	68.9	0.3	6.0	6.6	0.6
184.03	73.2	73.0	0.2	6.3	6.5	0.2
189.66	77.4	77.4	0.0	6.8	7.2	0.4
195.18	81.3	81.1	0.2	6.3	6.5	0.2
200.61	85.4	85.5	0.1	6.6	7.4	0.8
205.95	89.4	89.1	0.3	6.9	6.9	0.0
211.19	93.5	93.9	0.4	6.8	6.9	0.1
216.36	97.5	97.6	0.1	7.0	7.0	0.0
221.45	101.3	100.9	0.4	7.0	7.6	0.6
226.46	105.6	105.6	0.1	7.1	7.4	0.3
231.34	109.5	109.6	0.1	7.0	7.6	0.6
236.22	113.5	113.3	0.2	7.6	7.7	0.1
241.03	117.5	117.1	0.4	7.1	7.6	0.5
245.79	121.5	121.6	0.1	7.1	7.5	0.4
250.51	125.6	125.8	0.1	7.4	8.2	0.8
255.17	129.4	129.3	0.2	7.4	8.0	0.6
259.75	133.6	133.7	0.2	7.2	8.3	1.1
264.33	137.7	137.6	0.0	7.9	8.3	0.4
268.86	141.6	141.5	0.1	8.2	8.0	0.2
273.34	145.6	145.6	0.0	7.6	8.5	0.9
277.77	149.7	149.8	0.2	7.5	8.3	0.8
Average			0.2			0.5

Table 6.1: Ranges and Full Width at Half Maximums (FWHM) of the 21 used beams in the machine used in matRad and their corresponding simulated beam in TOPAS. The undertexts $_{MC}$ and $_{mR}$ refer to TOPAS Monte Carlo simulations and matRad values, accordingly.

6.3 Errors due to missassignments

The initial goal was to develop a treatment plan for carbon ions, hence the validation on the previous chapter, but due to time constraints that was not possible, Appendix (B) further explains these issues.

Because of this the analysis for carbon ion beams was reduced to comparing the ranges and FWHMs of the validated beams which would be used on the treatment plan trough phantoms of water, water-like muscle and water-like adipose tissue similar to section (3.2), the definitions of water-like muscle and water-like adipose tissue can be once again seen in Table 3.1.

In Figure 6.5, the behaviour of 5 beams of different energies can be seen, the dose profile near the entrance and at the fragmentation tails is somewhat rocky, once again this is due to time constraints, the number of histories for each simulation had to be reduced so that the data could be acquired in a reasonable amount of time, despite this in the more relevant area around the Bragg Peak the dose is still smooth. The values for range and FWHM as well as the differences for water-like muscle and water-like adipose tissue phantoms are in Tables (6.2) and (6.3), respectively. As expected the differences in range increase as the range increases, more range means more voxels to go through and the impacts of missassignments are larger. The differences in range are very similar to the ones obtained for proton beams of comparable ranges (Figure 3.3), for a range close to 105 mm the differences for protons were 0.8 mm and 0.4 mm for water-like muscle and water-like adipose tissue, respectively, and for ^{12}C ions these differences were 0.7 mm and 0.4 mm.

Energy(MeV)	R80$_{\mathrm{H2O}}$	R80$_{\mathrm{Muscle}}$(mm)	Δ R80(mm)	FWHM$_{\mathrm{H2O}}$(mm)	FWHM$_{\mathrm{Muscle}}$(mm)	Δ FWHM(mm)
178.28	69.2	69.7	0.5	6.0	6.1	0.1
184.03	73.2	73.7	0.5	6.3	6.5	0.2
189.66	77.4	78.0	0.6	6.8	6.9	0.1
195.18	81.3	81.9	0.6	6.3	6.5	0.2
200.61	85.4	86.1	0.7	6.6	7.0	0.4
205.95	89.4	90.0	0.6	6.9	7.0	0.1
211.19	93.5	94.2	0.7	6.8	6.7	0.1
216.36	97.5	98.3	0.8	7.0	7.1	0.1
221.45	101.3	102.1	0.8	7.0	7.4	0.4
226.46	105.6	106.3	0.7	7.1	7.0	0.1
231.34	109.5	110.3	0.8	7.0	7.1	0.1
236.22	113.5	114.3	0.8	7.6	7.7	0.1
241.03	117.5	118.3	0.8	7.1	7.0	0.1
245.79	121.5	122.5	1.0	7.1	7.0	0.1
250.51	125.6	126.6	1.0	7.4	7.7	0.3
255.17	129.4	130.5	1.1	7.4	7.7	0.3
259.75	133.6	134.6	1.0	7.2	7.2	0.0
264.33	137.7	138.7	1.0	7.9	8.0	0.1
268.86	141.6	142.7	1.1	8.2	8.4	0.2
273.34	145.6	146.8	1.2	7.6	7.1	0.5
277.77	149.7	150.9	1.2	7.5	7.6	0.1

Table 6.2: Differences in ranges and Full Width at Half Maximums (FWHM) of the 21 validated beams while travelling through a water or water-like muscle phantom.

Energy(MeV)	R80$_{\mathrm{H2O}}$	R80$_{\mathrm{Adipose}}$(mm)	Δ R80(mm)	FWHM$_{\mathrm{H2O}}$(mm)	FWHM$_{\mathrm{Adipose}}$(mm)	Δ FWHM(mm)
178.28	69.2	69.0	0.2	6.0	6.4	0.4
184.03	73.2	73.0	0.3	6.3	6.7	0.4
189.66	77.4	77.1	0.3	6.8	7.1	0.3
195.18	81.3	81.0	0.3	6.3	6.7	0.4
200.61	85.4	85.1	0.4	6.6	6.8	0.2
205.95	89.4	89.1	0.3	6.9	7.1	0.2
211.19	93.5	93.2	0.3	6.8	7.0	0.2
216.36	97.5	97.2	0.3	7.0	7.3	0.3
221.45	101.3	101.0	0.3	7.0	7.3	0.3
226.46	105.6	105.2	0.4	7.1	7.2	0.1
231.34	109.5	109.1	0.4	7.0	7.3	0.3
236.22	113.5	113.1	0.4	7.6	8.1	0.5
241.03	117.5	117.1	0.4	7.1	7.4	0.3
245.79	121.5	121.1	0.4	7.1	7.2	0.1
250.51	125.6	125.2	0.4	7.4	8.0	0.6
255.17	129.4	129.0	0.4	7.4	7.9	0.5
259.75	133.6	133.2	0.4	7.2	7.5	0.3
264.60	137.7	137.2	0.5	7.9	7.7	0.2
268.86	141.6	141.2	0.4	8.2	8.5	0.3
273.34	145.6	145.2	0.4	7.6	7.2	0.4
277.77	149.7	149.2	0.5	7.5	7.6	0.1

Table 6.3: Differences in ranges and Full Width at Half Maximums (FWHM) of the 21 validated beams while travelling through a water or water-like adipose tissue phantom.

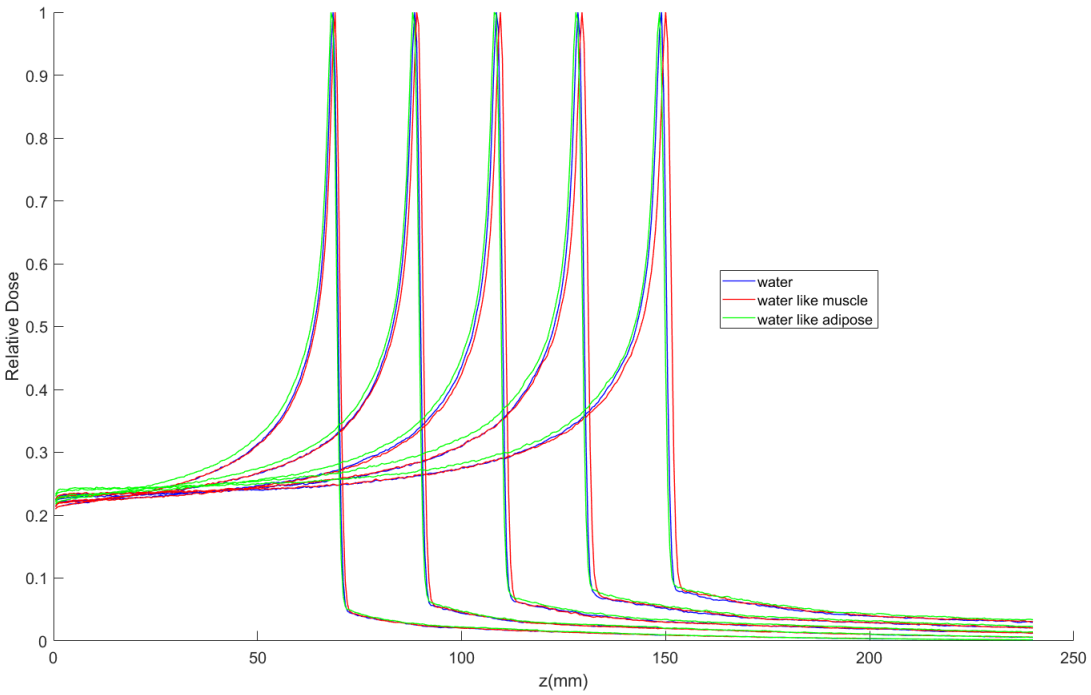

Figure 6.5: Comparison Comparison of depth dose distributions between beams of 178.28 MeV/u, 205.95 MeV/u, 231.34 MeV/u, 255.17 MeV/u and 277.77 MeV/u, from left to right, travelling through water, water-like muscle and water-like adipose tissue phantoms. Water-like muscle and water-like adipose tissue are, respectively, materials with the composition of muscle or adipose tissue but with the density and mean excitation energy of water. Each beam is normalized to its maximum.

Chapter 7

Comparison between therapies

Having simulated the behaviours of beams of both proton and ^{12}C ions and a treatment plan for protons all while analyzing and quantifying the errors due to tissue missassignments in the CT a comparison between each therapy can be made, also including photon therapy, looking at different parameters. A summary of this comparison can be seen in Table 7.1.

Photons are the easier particle to plan as they interact less with the body while carbon ions are the most complex it is needed to take into account both the fragmentation tail and the varying values of RBE. ^{12}C ion beams have the smallest penumbra, ^{12}C ions are heavier than protons so the effects of MCS have less effect on the sharpness of the beam, while photon beams have the highest (until about 15 cm where proton beams, due to MCS interaction deteriorating the sharpness of the beam, see their penumbra raise above the one of photons) as can be seen in Figure 6.1. Carbon ions distal falloff is also sharper than the one of protons and the FWHM of carbon stays almost constant as the range increases while for protons it increases much more prominently. The differences due to missassignments in the CT for generic beams of comparable ranges were nearly similar for proton and carbon ions. Photons have lower RBE while carbon ions have the highest, meaning carbon ion beams will do more damage to both tumour and healthy cells. Despite making it more effective it also becomes more complex to plan as a mistake in planning will lead to higher damage to healthy tissues.

It isimportant to consider is the potential for improvement in each therapy. It has been argued that proton therapy has a higher ceiling than conventional radiotherapy[22]. For the reasons previously listed it can be concluded that carbon ion therapy has an even higher potential.

In terms of cost, heavier particles are harder to accelerate therefore ^{12}C ion therapy will be the most expensive. Carbon ion therapy is also the most time consuming in terms of planning a treatment, not only from the fact that the planning itself is more complex but also if MC simulations are to be used said simulations take much longer than a similar situation for protons.

Particle	Photons	Protons	Carbon Ions
Planning (difficulty)	Easiest	Medium	Hardest
Penumbra($<$15 cm depth)	Worst	Medium	Best
Penumbra ($>$15 cm depth)	Medium	Worst	Best
Distal Falloff	——	Sharp	Sharpest
Relative biological effectiveness	1	0.7-1.6	1-3.5
Time consumed	Lower	Medium	Highest
Potential ceiling	Lower	High	Highest
Price	Cheapest	Medium	Most expensive

Table 7.1: Comparison between characteristics for each particle therapy.

Chapter 8

Conclusions and future work

Uncertainties in proton therapy are much more severe than in photon radiotherapy due to the finite range of the particles. Missassignment errors in the CT of a patient are one cause for these uncertainties in range.

Under this thesis, the impact of these errors on the range of the dose was calculated for a variety of configurations using Monte Carlo simulations.

The first setup were generic proton beams with energies of 80 MeV, 120 MeV, 160 MeV, 200 MeV and 240 MeV travelling through a homogeneous cubic phantom. The errors were introduced by changing the composition of the phantom from water to water-like muscle and water-like adipose tissue, these virtual tissues have the the composition of muscle or adipose, respectively, but are assigned the density of water. The differences in range were all below 1% and grow as the energy rises, as expected since the beam travels through a greater depth and the differences in material have a larger impact on the loss of energy.

The process of creating a treatment plan with particle therapy requires defining several parameters that follow detailed clinical protocols which depend on the type of particle, beam, machine and even center. The treatment plan is calculated by complex algorithms that manipulate parameters such as spot position and size as well as beam energy and weight to achieve the best possible dose to the target while minimizing dose delivered to the surrounding volumes. To calculate these parameters matRad, an open source code based on MATLAB, was used. The beams to be used in TOPAS were validated with an average range difference of (0.4$\pm$0.3) mm.

A treatment for a brain tumour of a pediatric patient was developed. In this chapter segmentation errors were introduced by modifying the method of conversion from Hounsfield Units (HU), in the CT to densities and compositions so that voxels of the CT with either muscle or adipose kept their composition but were assigned the density of water. This was done by introducing a correction factor to the density formula.

The average difference in range due to these errors was 3.5 mm (2.6% of the range) with a standard deviation of 0.4 mm. This value of 2.6% is higher than the estimation made in [15] of 1.7% but it must be kept in mind that the value obtained here was the worst case scenario where the errors were introduced into all voxels. If the margins for a treatment plan are to be defined in the most conservative way possible the contribution due to missassignments in the CT numbers should be 3.9 mm (the upper value of the average plus the standard deviation)

The same treatment plan was to be developed for carbon ions so the necessary beams were validated and had an average range difference of (0.2$\pm$0.1)mm.

Due to time constraints caused by the long computational time of carbon ion beams the treatment plan was not able to be developed, despite this taking into account both the validation and the physics of

these beams it is expected that the difference in range would be similar or inferior to the one calculated for protons.

A comparison was made between each therapy where it was concluded that while carbon ion therapy has the highest potential to deliver a uniform dose alongside being easier on the patient, this therapy is also the most expensive as well as most complex and time consuming to plan.

Because of time limitations the simulation for the treatment plan using carbon ions was not possible therefore future work could include this simulation as well similar simulations for different sized tumours located in different areas since the differences in range will be affected both by the size and location of the tumour and the traversed tissues. If someone else was to further develop this research, it should be noted that a barrier would be the development of the scripts that both create the parameter files and analyze the data. This work took place ”behind the scenes” but was very complex and integral to the thesis.

References

[1] In: *World Health Organization* (2020). URL: https://www.who.int/en/news-room/fact-sheets/detail/cancer.

[2] In: *Global Cancer Observatory* (2020). URL: https://gco.iarc.fr/today/data/factsheets/cancers/39-All-cancers-fact-sheet.pdf.

[3] 2020. URL: https://www.iarc.fr/wp-content/uploads/2018/07/wcr-6.pdf.

[4] Scott Tyldesley, Geoff Delaney, Farshad Foroudi, Lisa Barbera, Marc Kerba, and William Mackillop. "Estimating the Need for Radiotherapy for Patients With Prostate, Breast, and Lung Cancers: Verification of Model Estimates of Need With Radiotherapy Utilization Data From British Columbia". In: *International Journal of Radiation Oncology*Biology*Physics* 79.5 (2011), pp. 1507–1515. ISSN: 0360-3016. DOI: https://doi.org/10.1016/j.ijrobp.2009.12.070.

[5] In: *Global Cancer Observatory* (2020). URL: https://gco.iarc.fr/today/data/factsheets/populations/620-portugal-fact-sheets.pdf.

[6] In: *Particle Therapy Co-Operative Group* (2020). URL: https://www.ptcog.ch/index.php/facilities-in-operation.

[7] Stanley I. Gutiontov, Edward J. Shin, Benjamin Lok, Nancy Y. Lee, and Ruben Cabanillas. "Intensity-modulated radiotherapy for head and neck surgeons". In: *Head & Neck* 38.S1 (), E2368–E2373. DOI: 10.1002/hed.24338.

[8] Wayne D Newhauser and Rui Zhang. "The physics of proton therapy". In: *Physics in Medicine and Biology* 60.8 (Mar. 2015), R155–R209. DOI: 10.1088/0031-9155/60/8/r155.

[9] Saaidi and Cherkaoui El Moursly R. *Monte Carlo Study of Photon Dose Distributions Produced By 12 MV Linear Accelerator*. Aug. 2018. URL: https://symbiosisonlinepublishing.com/biosensors-biomarkers-diagnostics/biosensors-biomarkers-diagnostics20.php.

[10] Antony Lomax. *Charged Particle Therapy: The Physics of Interaction*. DOI: 10.1097/PPO.0b013e3181af5cc7.

[11] Bryan Bednarz, Juliane Daartz, and Harald Paganetti. "Dosimetric accuracy of planning and delivering small proton therapy fields". In: *Physics in Medicine and Biology* 55.24 (Nov. 2010), pp. 7425–7438. DOI: 10.1088/0031-9155/55/24/003.

[12] S. Agostinelli et al. "Geant4—a simulation toolkit". In: *Nuclear Instruments and Methods in Physics Research Section A: Accelerators, Spectrometers, Detectors and Associated Equipment* 506.3 (2003), pp. 250–303. ISSN: 0168-9002. DOI: https://doi.org/10.1016/S0168-9002(03)01368-8.

[13] "TOPAS MC". In: (2020). URL: http://www.topasmc.org/.

[14] J. Perl, J. Shin, J. Schümann, B. Faddegon, and H. Paganetti. "TOPAS: An innovative proton Monte Carlo platform for research and clinical applications". In: *Medical Physics* 39.11 (2012), pp. 6818–6837. DOI: 10.1118/1.4758060.

[15] Harald Paganetti. "Range uncertainties in proton therapy and the role of Monte Carlo simulations". In: *Physics in Medicine and Biology* 57.11 (May 2012), R99–R117. DOI: 10.1088/0031-9155/57/11/r99.

[16] Thomas Bortfeld. "An analytical approximation of the Bragg curve for therapeutic proton beams". In: *Medical Physics* 24.12 (1997), pp. 2024–2033. DOI: 10.1118/1.598116.

[17] In: *World Cancer Report* (2020). URL: https://publications.iarc.fr/586.

[18] Wilfried Schneider, Thomas Bortfeld, and Wolfgang Schlegel. “Correlation between CT numbers and tissue parameters needed for Monte Carlo simulations of clinical dose distributions”. In: *Physics in medicine and biology* 45 (Mar. 2000), pp. 459–78. DOI: 10.1088/0031-9155/45/2/314.

[19] DR White, HQ Woodard, and SM Hammond. “Average soft-tissue and bone models for use in radiation dosimetry”. In: *The British journal of radiology* 60.717 (Sept. 1987), pp. 907–913. ISSN: 0007-1285. DOI: 10.1259/0007-1285-60-717-907.

[20] Herman Suit, Thomas DeLaney, Saveli Goldberg, Harald Paganetti, Ben Clasie, Leo Gerweck, Andrzej Niemierko, Eric Hall, Jacob Flanz, Josh Hallman, and et al. *Proton vs carbon ion beams in the definitive radiation treatment of cancer patients*. Apr. 2010. URL: https://www.ncbi.nlm.nih.gov/pubmed/20185186.

[21] Harald Paganetti and Peter van Luijk. “Biological Considerations When Comparing Proton Therapy With Photon Therapy”. In: *Seminars in Radiation Oncology* 23.2 (2013), pp. 77–87. ISSN: 1053-4296. DOI: https://doi.org/10.1016/j.semradonc.2012.11.002.

[22] Harald Paganetti, Cedric X. Yu, and Colin G. Orton. “Photon radiotherapy has reached its limit in terms of catching up dosimetrically with proton therapy”. In: *Medical Physics* 43.8Part1 (2016), pp. 4470–4472. DOI: 10.1118/1.4954790.

Appendix A

TOPAS parameter file

For a better understanding of how a TOPAS parameter file is setup for the treatment plans simulated in this work this appendix will analyze one of these files by going trough what each section and line represents. The parameter file does not fit into a single page so it will be divided into different images.

Line number 2 defines how many threads are used in the simulation, while the PC has 16 threads not all of them can be used due to RAM limitations since each additional thread requires a duplicate of the geometry components and scoring grid. Lines 4 to 32 fetch the beam parameters for all used beams from parameter files which have the information of the characteristics of the corresponding beam. Lines 34, 35 and 36 define how many sequential steps the simulation will have, this sets up how many different configurations will be used and the rate at which parameters change during the simulation. Lines 38 to 43 define every scan spot for the pencil beam scanning, these are relative to the isocenter of the simulation. Lines 44 to 49 move the source of the beam to the corresponding scan spot. Lines 50 to 97 are the continuation of Figure A.1 move the source of the beam to the corresponding scan spot, each beam is being moved separately. Lines 98 trough 130 are a continuation of Figure A.2 to move the remainder of the beams. Lines 132 to 145 define how the number of histories for each beam will change. Lines 146 to 160 are a continuation of Figure A.4and define how the number of histories for each remaining beam will change. Lines 161 to 189 define the step of the change of histories for each beam. Lines 190 to 193 define the number of histories in each run for each scan spot, these lines are too big to fully show here, there is an integer for each scan spot that represents the relative weight of the corresponding beam for each scan spot, this is the number of primary particles that will be sent from each beam for each scan spot. Lines 194 to 218 are a continuation of Figure A.4 for the remaining beams. Lines 219 to 241 set the number of histories to change according to the previous parameters from line 190 to line 218. Lines 242 to are a continuation of Figure A.5 for the remainder of the beams. Line 249 includes the information for the conversion of the Hounsfield units from the CT to densities and compositions for each voxel according to the model discussed in section (5.2.2). Line 250 defines where the patient will be setup in relation to the World, this parameter for each of the beams is ”hidden” since it is in the files which are included in Figure A.1. Line 251 initializes the composition of the patient which is changed afterwards. Lines 261, 262 and 263 transition the patient to have it located in the correct position relative to its isocenter. Lines 264, 265 and 266 rotate the patient, in an actual clinic both the gantry and couch move, here it is easier and equivalent of course to just rotate the patient. Line 267 defines that the CT is in DICOM format and line 268 has the directory in which the CT is. Line 270 defines the quantity scored, in this case the dose delivered to the medium which is the patient, this is defined in line 271. Line 272 allows to overwrite the output file if it already exists and line 273 defines the format of the output file, in this case the DICOM format.

```
i:Ts/NumberOfThreads = 9
#####Used Beams
includeFile=../validation/position_9_try.txt
includeFile=../validation/position_10_try.txt
includeFile=../validation/position_11_try.txt
includeFile=../validation/position_12_try.txt
includeFile=../validation/position_13_try.txt
includeFile=../validation/position_14_try.txt
includeFile=../validation/position_15_try.txt
includeFile=../validation/position_16_try.txt
includeFile=../validation/position_17_try.txt
includeFile=../validation/position_18_try.txt
includeFile=../validation/position_19_try.txt
includeFile=../validation/position_20_try.txt
includeFile=../validation/position_21_try.txt
includeFile=../validation/position_22_try.txt
includeFile=../validation/position_23_try.txt
includeFile=../validation/position_24_try.txt
includeFile=../validation/position_25_try.txt
includeFile=../validation/position_26_try.txt
includeFile=../validation/position_27_try.txt
includeFile=../validation/position_28_try.txt
includeFile=../validation/position_29_try.txt
includeFile=../validation/position_30_try.txt
includeFile=../validation/position_31_try.txt
includeFile=../validation/position_32_try.txt
includeFile=../validation/position_33_try.txt
includeFile=../validation/position_34_try.txt
includeFile=../validation/position_35_try.txt
includeFile=../validation/position_36_try.txt
includeFile=../validation/position_37_try.txt
#####Timeline
d:Tf/TimelineStart = 0.0 s
d:Tf/TimelineEnd = 160.0 s
i:Tf/NumberOfSequentialTimes = 160
#####Get the Positions
s:Tf/PositionsX/Function = "Step"
dv:Tf/PositionsX/Times = 160 1 2 3 4 5 6 7 8 9 10 11 12 13 14
dv:Tf/PositionsX/Values = 160 -35 -35 -35 -35 -30 -30 -30 -30
s:Tf/PositionsY/Function = "Step"
dv:Tf/PositionsY/Times = 160 1 2 3 4 5 6 7 8 9 10 11 12 13 14
dv:Tf/PositionsY/Values = 160 -5   0   5  10 -20 -15 -10  -5
d:Ge/myBeam9Position/TransX = Tf/PositionsX/Value  mm
d:Ge/myBeam9Position/TransY = Tf/PositionsY/Value  mm
#d:Ge/myBeam9Position/TransZ = Ge/IsoCenterY - 2500  mm
d:Ge/myBeam10Position/TransX = Tf/PositionsX/Value  mm
d:Ge/myBeam10Position/TransY = Tf/PositionsY/Value  mm
#d:Ge/myBeam10Position/TransZ = Ge/IsoCenterY - 2500  mm
```

Figure A.1: Lines 2 to 49

```
50  d:Ge/myBeam11Position/TransX = Tf/PositionsX/Value  mm
51  d:Ge/myBeam11Position/TransY = Tf/PositionsY/Value  mm
52  #d:Ge/myBeam11Position/TransZ = Ge/IsoCenterY - 2500  mm
53  d:Ge/myBeam12Position/TransX = Tf/PositionsX/Value  mm
54  d:Ge/myBeam12Position/TransY = Tf/PositionsY/Value  mm
55  #d:Ge/myBeam12Position/TransZ = Ge/IsoCenterY - 2500  mm
56  d:Ge/myBeam13Position/TransX = Tf/PositionsX/Value  mm
57  d:Ge/myBeam13Position/TransY = Tf/PositionsY/Value  mm
58  #d:Ge/myBeam13Position/TransZ = Ge/IsoCenterY - 2500  mm
59  d:Ge/myBeam14Position/TransX = Tf/PositionsX/Value  mm
60  d:Ge/myBeam14Position/TransY = Tf/PositionsY/Value  mm
61  #d:Ge/myBeam14Position/TransZ = Ge/IsoCenterY - 2500  mm
62  d:Ge/myBeam15Position/TransX = Tf/PositionsX/Value  mm
63  d:Ge/myBeam15Position/TransY = Tf/PositionsY/Value  mm
64  #d:Ge/myBeam15Position/TransZ = Ge/IsoCenterY - 2500  mm
65  d:Ge/myBeam16Position/TransX = Tf/PositionsX/Value  mm
66  d:Ge/myBeam16Position/TransY = Tf/PositionsY/Value  mm
67  #d:Ge/myBeam16Position/TransZ = Ge/IsoCenterY - 2500  mm
68  d:Ge/myBeam17Position/TransX = Tf/PositionsX/Value  mm
69  d:Ge/myBeam17Position/TransY = Tf/PositionsY/Value  mm
70  #d:Ge/myBeam17Position/TransZ = Ge/IsoCenterY - 2500  mm
71  d:Ge/myBeam18Position/TransX = Tf/PositionsX/Value  mm
72  d:Ge/myBeam18Position/TransY = Tf/PositionsY/Value  mm
73  #d:Ge/myBeam18Position/TransZ = Ge/IsoCenterY - 2500  mm
74  d:Ge/myBeam19Position/TransX = Tf/PositionsX/Value  mm
75  d:Ge/myBeam19Position/TransY = Tf/PositionsY/Value  mm
76  #d:Ge/myBeam19Position/TransZ = Ge/IsoCenterY - 2500  mm
77  d:Ge/myBeam20Position/TransX = Tf/PositionsX/Value  mm
78  d:Ge/myBeam20Position/TransY = Tf/PositionsY/Value  mm
79  #d:Ge/myBeam20Position/TransZ = Ge/IsoCenterY - 2500  mm
80  d:Ge/myBeam21Position/TransX = Tf/PositionsX/Value  mm
81  d:Ge/myBeam21Position/TransY = Tf/PositionsY/Value  mm
82  #d:Ge/myBeam21Position/TransZ = Ge/IsoCenterY - 2500  mm
83  d:Ge/myBeam22Position/TransX = Tf/PositionsX/Value  mm
84  d:Ge/myBeam22Position/TransY = Tf/PositionsY/Value  mm
85  #d:Ge/myBeam22Position/TransZ = Ge/IsoCenterY - 2500  mm
86  d:Ge/myBeam23Position/TransX = Tf/PositionsX/Value  mm
87  d:Ge/myBeam23Position/TransY = Tf/PositionsY/Value  mm
88  #d:Ge/myBeam23Position/TransZ = Ge/IsoCenterY - 2500  mm
89  d:Ge/myBeam24Position/TransX = Tf/PositionsX/Value  mm
90  d:Ge/myBeam24Position/TransY = Tf/PositionsY/Value  mm
91  #d:Ge/myBeam24Position/TransZ = Ge/IsoCenterY - 2500  mm
92  d:Ge/myBeam25Position/TransX = Tf/PositionsX/Value  mm
93  d:Ge/myBeam25Position/TransY = Tf/PositionsY/Value  mm
94  #d:Ge/myBeam25Position/TransZ = Ge/IsoCenterY - 2500  mm
95  d:Ge/myBeam26Position/TransX = Tf/PositionsX/Value  mm
96  d:Ge/myBeam26Position/TransY = Tf/PositionsY/Value  mm
97  #d:Ge/myBeam26Position/TransZ = Ge/IsoCenterY - 2500  mm
```

Figure A.2: Lines 50 to 97.

```
 98   d:Ge/myBeam27Position/TransX = Tf/PositionsX/Value  mm
 99   d:Ge/myBeam27Position/TransY = Tf/PositionsY/Value  mm
100   #d:Ge/myBeam27Position/TransZ = Ge/IsoCenterY - 2500  mm
101   d:Ge/myBeam28Position/TransX = Tf/PositionsX/Value  mm
102   d:Ge/myBeam28Position/TransY = Tf/PositionsY/Value  mm
103   #d:Ge/myBeam28Position/TransZ = Ge/IsoCenterY - 2500  mm
104   d:Ge/myBeam29Position/TransX = Tf/PositionsX/Value  mm
105   d:Ge/myBeam29Position/TransY = Tf/PositionsY/Value  mm
106   #d:Ge/myBeam29Position/TransZ = Ge/IsoCenterY - 2500  mm
107   d:Ge/myBeam30Position/TransX = Tf/PositionsX/Value  mm
108   d:Ge/myBeam30Position/TransY = Tf/PositionsY/Value  mm
109   #d:Ge/myBeam30Position/TransZ = Ge/IsoCenterY - 2500  mm
110   d:Ge/myBeam31Position/TransX = Tf/PositionsX/Value  mm
111   d:Ge/myBeam31Position/TransY = Tf/PositionsY/Value  mm
112   #d:Ge/myBeam31Position/TransZ = Ge/IsoCenterY - 2500  mm
113   d:Ge/myBeam32Position/TransX = Tf/PositionsX/Value  mm
114   d:Ge/myBeam32Position/TransY = Tf/PositionsY/Value  mm
115   #d:Ge/myBeam32Position/TransZ = Ge/IsoCenterY - 2500  mm
116   d:Ge/myBeam33Position/TransX = Tf/PositionsX/Value  mm
117   d:Ge/myBeam33Position/TransY = Tf/PositionsY/Value  mm
118   #d:Ge/myBeam33Position/TransZ = Ge/IsoCenterY - 2500  mm
119   d:Ge/myBeam34Position/TransX = Tf/PositionsX/Value  mm
120   d:Ge/myBeam34Position/TransY = Tf/PositionsY/Value  mm
121   #d:Ge/myBeam34Position/TransZ = Ge/IsoCenterY - 2500  mm
122   d:Ge/myBeam35Position/TransX = Tf/PositionsX/Value  mm
123   d:Ge/myBeam35Position/TransY = Tf/PositionsY/Value  mm
124   #d:Ge/myBeam35Position/TransZ = Ge/IsoCenterY - 2500  mm
125   d:Ge/myBeam36Position/TransX = Tf/PositionsX/Value  mm
126   d:Ge/myBeam36Position/TransY = Tf/PositionsY/Value  mm
127   #d:Ge/myBeam36Position/TransZ = Ge/IsoCenterY - 2500  mm
128   d:Ge/myBeam37Position/TransX = Tf/PositionsX/Value  mm
129   d:Ge/myBeam37Position/TransY = Tf/PositionsY/Value  mm
130   #d:Ge/myBeam37Position/TransZ = Ge/IsoCenterY - 2500  mm
131   #####Get the Weights
132   s:Tf/Weights9/Function = "Step"
133   s:Tf/Weights10/Function = "Step"
134   s:Tf/Weights11/Function = "Step"
135   s:Tf/Weights12/Function = "Step"
136   s:Tf/Weights13/Function = "Step"
137   s:Tf/Weights14/Function = "Step"
138   s:Tf/Weights15/Function = "Step"
139   s:Tf/Weights16/Function = "Step"
140   s:Tf/Weights17/Function = "Step"
141   s:Tf/Weights18/Function = "Step"
142   s:Tf/Weights19/Function = "Step"
143   s:Tf/Weights20/Function = "Step"
144   s:Tf/Weights21/Function = "Step"
145   s:Tf/Weights22/Function = "Step"
```

Figure A.3: Lines 98 to 145.

```
146   s:Tf/Weights23/Function = "Step"
147   s:Tf/Weights24/Function = "Step"
148   s:Tf/Weights25/Function = "Step"
149   s:Tf/Weights26/Function = "Step"
150   s:Tf/Weights27/Function = "Step"
151   s:Tf/Weights28/Function = "Step"
152   s:Tf/Weights29/Function = "Step"
153   s:Tf/Weights30/Function = "Step"
154   s:Tf/Weights31/Function = "Step"
155   s:Tf/Weights32/Function = "Step"
156   s:Tf/Weights33/Function = "Step"
157   s:Tf/Weights34/Function = "Step"
158   s:Tf/Weights35/Function = "Step"
159   s:Tf/Weights36/Function = "Step"
160   s:Tf/Weights37/Function = "Step"
161   dv:Tf/Weights9/Times = 160 1 2 3 4 5 6 7 8 9 10 11 12 13 14 15 16 17 18 19 20 21 2
162   dv:Tf/Weights10/Times = 160 1 2 3 4 5 6 7 8 9 10 11 12 13 14 15 16 17 18 19 20 21
163   dv:Tf/Weights11/Times = 160 1 2 3 4 5 6 7 8 9 10 11 12 13 14 15 16 17 18 19 20 21
164   dv:Tf/Weights12/Times = 160 1 2 3 4 5 6 7 8 9 10 11 12 13 14 15 16 17 18 19 20 21
165   dv:Tf/Weights13/Times = 160 1 2 3 4 5 6 7 8 9 10 11 12 13 14 15 16 17 18 19 20 21
166   dv:Tf/Weights14/Times = 160 1 2 3 4 5 6 7 8 9 10 11 12 13 14 15 16 17 18 19 20 21
167   dv:Tf/Weights15/Times = 160 1 2 3 4 5 6 7 8 9 10 11 12 13 14 15 16 17 18 19 20 21
168   dv:Tf/Weights16/Times = 160 1 2 3 4 5 6 7 8 9 10 11 12 13 14 15 16 17 18 19 20 21
169   dv:Tf/Weights17/Times = 160 1 2 3 4 5 6 7 8 9 10 11 12 13 14 15 16 17 18 19 20 21
170   dv:Tf/Weights18/Times = 160 1 2 3 4 5 6 7 8 9 10 11 12 13 14 15 16 17 18 19 20 21
171   dv:Tf/Weights19/Times = 160 1 2 3 4 5 6 7 8 9 10 11 12 13 14 15 16 17 18 19 20 21
172   dv:Tf/Weights20/Times = 160 1 2 3 4 5 6 7 8 9 10 11 12 13 14 15 16 17 18 19 20 21
173   dv:Tf/Weights21/Times = 160 1 2 3 4 5 6 7 8 9 10 11 12 13 14 15 16 17 18 19 20 21
174   dv:Tf/Weights22/Times = 160 1 2 3 4 5 6 7 8 9 10 11 12 13 14 15 16 17 18 19 20 21
175   dv:Tf/Weights23/Times = 160 1 2 3 4 5 6 7 8 9 10 11 12 13 14 15 16 17 18 19 20 21
176   dv:Tf/Weights24/Times = 160 1 2 3 4 5 6 7 8 9 10 11 12 13 14 15 16 17 18 19 20 21
177   dv:Tf/Weights25/Times = 160 1 2 3 4 5 6 7 8 9 10 11 12 13 14 15 16 17 18 19 20 21
178   dv:Tf/Weights26/Times = 160 1 2 3 4 5 6 7 8 9 10 11 12 13 14 15 16 17 18 19 20 21
179   dv:Tf/Weights27/Times = 160 1 2 3 4 5 6 7 8 9 10 11 12 13 14 15 16 17 18 19 20 21
180   dv:Tf/Weights28/Times = 160 1 2 3 4 5 6 7 8 9 10 11 12 13 14 15 16 17 18 19 20 21
181   dv:Tf/Weights29/Times = 160 1 2 3 4 5 6 7 8 9 10 11 12 13 14 15 16 17 18 19 20 21
182   dv:Tf/Weights30/Times = 160 1 2 3 4 5 6 7 8 9 10 11 12 13 14 15 16 17 18 19 20 21
183   dv:Tf/Weights31/Times = 160 1 2 3 4 5 6 7 8 9 10 11 12 13 14 15 16 17 18 19 20 21
184   dv:Tf/Weights32/Times = 160 1 2 3 4 5 6 7 8 9 10 11 12 13 14 15 16 17 18 19 20 21
185   dv:Tf/Weights33/Times = 160 1 2 3 4 5 6 7 8 9 10 11 12 13 14 15 16 17 18 19 20 21
186   dv:Tf/Weights34/Times = 160 1 2 3 4 5 6 7 8 9 10 11 12 13 14 15 16 17 18 19 20 21
187   dv:Tf/Weights35/Times = 160 1 2 3 4 5 6 7 8 9 10 11 12 13 14 15 16 17 18 19 20 21
188   dv:Tf/Weights36/Times = 160 1 2 3 4 5 6 7 8 9 10 11 12 13 14 15 16 17 18 19 20 21
189   dv:Tf/Weights37/Times = 160 1 2 3 4 5 6 7 8 9 10 11 12 13 14 15 16 17 18 19 20 21
190   iv:Tf/Weights9/Values= 160     0       0       0       0       0       0       0
191   iv:Tf/Weights10/Values= 160     0       0       0       0       0       0       0
192   iv:Tf/Weights11/Values= 160     0       0       0       0       0       0       0
193   iv:Tf/Weights12/Values= 160     0       0       0       0       0       0       0
```

Figure A.4: Lines 146 to 193.

```
194  iv:Tf/Weights13/Values= 160     0       0       0       0       0       0       0       0
195  iv:Tf/Weights14/Values= 160     0       0       0       0       0       0       0       0
196  iv:Tf/Weights15/Values= 160     0       0       0       0       0       0       0       0
197  iv:Tf/Weights16/Values= 160     0       0       0       0       0       0       0       0
198  iv:Tf/Weights17/Values= 160     0       0       0       0       0       0       0       0
199  iv:Tf/Weights18/Values= 160     0       0       0       0       0       0       0       0
200  iv:Tf/Weights19/Values= 160     0       0       0       0       0       0    6083    3983
201  iv:Tf/Weights20/Values= 160     0       0       0       0       0       0    7012    5408
202  iv:Tf/Weights21/Values= 160     0       0       0       0       0    5856    4704    2080
203  iv:Tf/Weights22/Values= 160     0       0       0       0       0    9575    9693    7257
204  iv:Tf/Weights23/Values= 160 34251   13294   17982   29753   18606   12208    5163      84
205  iv:Tf/Weights24/Values= 160 35648      98    5295   32234   20301   16157    3201      36
206  iv:Tf/Weights25/Values= 160 58940   13284   28457   61433   27192   16768      77       9
207  iv:Tf/Weights26/Values= 160     0  114928       0       0   42841   23662   17438       3
208  iv:Tf/Weights27/Values= 160     0       0       0       0       0   37812   26436   15412
209  iv:Tf/Weights28/Values= 160     0       0       0       0       0   39789   25935   14617
210  iv:Tf/Weights29/Values= 160     0       0       0       0       0   57652   44300   23632
211  iv:Tf/Weights30/Values= 160     0       0       0       0       0       0   66080   49544
212  iv:Tf/Weights31/Values= 160     0       0       0       0       0       0       0       0
213  iv:Tf/Weights32/Values= 160     0       0       0       0       0       0       0       0
214  iv:Tf/Weights33/Values= 160     0       0       0       0       0       0       0       0
215  iv:Tf/Weights34/Values= 160     0       0       0       0       0       0       0       0
216  iv:Tf/Weights35/Values= 160     0       0       0       0       0       0       0       0
217  iv:Tf/Weights36/Values= 160     0       0       0       0       0       0       0       0
218  iv:Tf/Weights37/Values= 160     0       0       0       0       0       0       0       0
219  i:So/myBeam9/NumberOfHistoriesInRun = Tf/Weights9/Value
220  i:So/myBeam10/NumberOfHistoriesInRun = Tf/Weights10/Value
221  i:So/myBeam11/NumberOfHistoriesInRun = Tf/Weights11/Value
222  i:So/myBeam12/NumberOfHistoriesInRun = Tf/Weights12/Value
223  i:So/myBeam13/NumberOfHistoriesInRun = Tf/Weights13/Value
224  i:So/myBeam14/NumberOfHistoriesInRun = Tf/Weights14/Value
225  i:So/myBeam15/NumberOfHistoriesInRun = Tf/Weights15/Value
226  i:So/myBeam16/NumberOfHistoriesInRun = Tf/Weights16/Value
227  i:So/myBeam17/NumberOfHistoriesInRun = Tf/Weights17/Value
228  i:So/myBeam18/NumberOfHistoriesInRun = Tf/Weights18/Value
229  i:So/myBeam19/NumberOfHistoriesInRun = Tf/Weights19/Value
230  i:So/myBeam20/NumberOfHistoriesInRun = Tf/Weights20/Value
231  i:So/myBeam21/NumberOfHistoriesInRun = Tf/Weights21/Value
232  i:So/myBeam22/NumberOfHistoriesInRun = Tf/Weights22/Value
233  i:So/myBeam23/NumberOfHistoriesInRun = Tf/Weights23/Value
234  i:So/myBeam24/NumberOfHistoriesInRun = Tf/Weights24/Value
235  i:So/myBeam25/NumberOfHistoriesInRun = Tf/Weights25/Value
236  i:So/myBeam26/NumberOfHistoriesInRun = Tf/Weights26/Value
237  i:So/myBeam27/NumberOfHistoriesInRun = Tf/Weights27/Value
238  i:So/myBeam28/NumberOfHistoriesInRun = Tf/Weights28/Value
239  i:So/myBeam29/NumberOfHistoriesInRun = Tf/Weights29/Value
240  i:So/myBeam30/NumberOfHistoriesInRun = Tf/Weights30/Value
241  i:So/myBeam31/NumberOfHistoriesInRun = Tf/Weights31/Value
```

Figure A.5: Lines 194 to 241.

```
242  i:So/myBeam32/NumberOfHistoriesInRun = Tf/Weights32/Value
243  i:So/myBeam33/NumberOfHistoriesInRun = Tf/Weights33/Value
244  i:So/myBeam34/NumberOfHistoriesInRun = Tf/Weights34/Value
245  i:So/myBeam35/NumberOfHistoriesInRun = Tf/Weights35/Value
246  i:So/myBeam36/NumberOfHistoriesInRun = Tf/Weights36/Value
247  i:So/myBeam37/NumberOfHistoriesInRun = Tf/Weights37/Value
248  ##########Importing CT
249  includeFile=HUtoMaterialSchneider_mine.txt
250  s:Ge/Patient/Parent="World"
251  s:Ge/Patient/Material="G4_WATER"
252  #d:Ge/IsoCenterX=-232.6 mm
253  #d:Ge/IsoCenterY=-243.6 mm
254  #d:Ge/IsoCenterZ=-147.7 mm
255  #dc:Ge/Patient/DicomOriginX=0.0 mm
256  #dc:Ge/Patient/DicomOriginY=0.0 mm
257  #dc:Ge/Patient/DicomOriginZ=0.0 mm
258  #d:Ge/Patient/TransX=Ge/IsoCenterX mm
259  #d:Ge/Patient/TransY=Ge/IsoCenterY mm
260  #d:Ge/Patient/TransZ=Ge/IsoCenterZ mm
261  d:Ge/Patient/TransX=12.4 mm
262  d:Ge/Patient/TransY=23.4 mm
263  d:Ge/Patient/TransZ=0.0 mm
264  d:Ge/Patient/RotX=0.0 deg
265  d:Ge/Patient/RotY=180.0 deg
266  d:Ge/Patient/RotZ=180.0 deg
267  s:Ge/Patient/Type="TsDicomPatient"
268  s:Ge/Patient/DicomDirectory="just_CT2"
269  ##########Scoring
270  s:Sc/DoseOnCTGrid270_14_mine_other/Quantity="DoseToMedium"
271  s:Sc/DoseOnCTGrid270_14_mine_other/Component="Patient"
272  s:Sc/DoseOnCTGrid270_14_mine_other/IfOutputFileAlreadyExists="Overwrite"
273  s:Sc/DoseOnCTGrid270_14_mine_other/OutputType="DICOM"
274  #i:Sc/DoseOnCTGrid270_14_mine/XBins=512
275  #i:Sc/DoseOnCTGrid270_14_mine/YBins=512
276  #i:Sc/DoseOnCTGrid270_14_mine/ZBins=534
```

Figure A.6: Lines 242 to 276

Appendix B

Carbon Ion Treatment Plan

As mentioned in section (6.3) due to time constraints the simulation of a correct treatment plan was not possible. Previous to this conclusion an attempt to simulate the treatment plan was made, the result can be seen in Figure B.1. The main issue which can be seen is that the dose is not constant, there are gaps, this happens because the scan spots were too far away from one another, another issue that is harder to detect is that the number of histories used was very low. The scan spots were 5 mm apart, to achieve a better result this distance would need to be reduced to at least half and to obtain statistically relevant data the number of histories would have to be at least 10 times higher, reducing the distance between scan spots to half would increase the simulation time by a factor 4 and ten times the histories would increase it by a factor of 10 (both are estimations), this would lead to a simulation of the treatment plan being 40 times more consuming, taking into account that the attempted simulation took around 2 days to finish, a relevant correct simulation would take 80 days, the fact that the carbon treatment plan was the final goal of the thesis along with this enormous time consumption lead to the impossibility of simulating the plan.

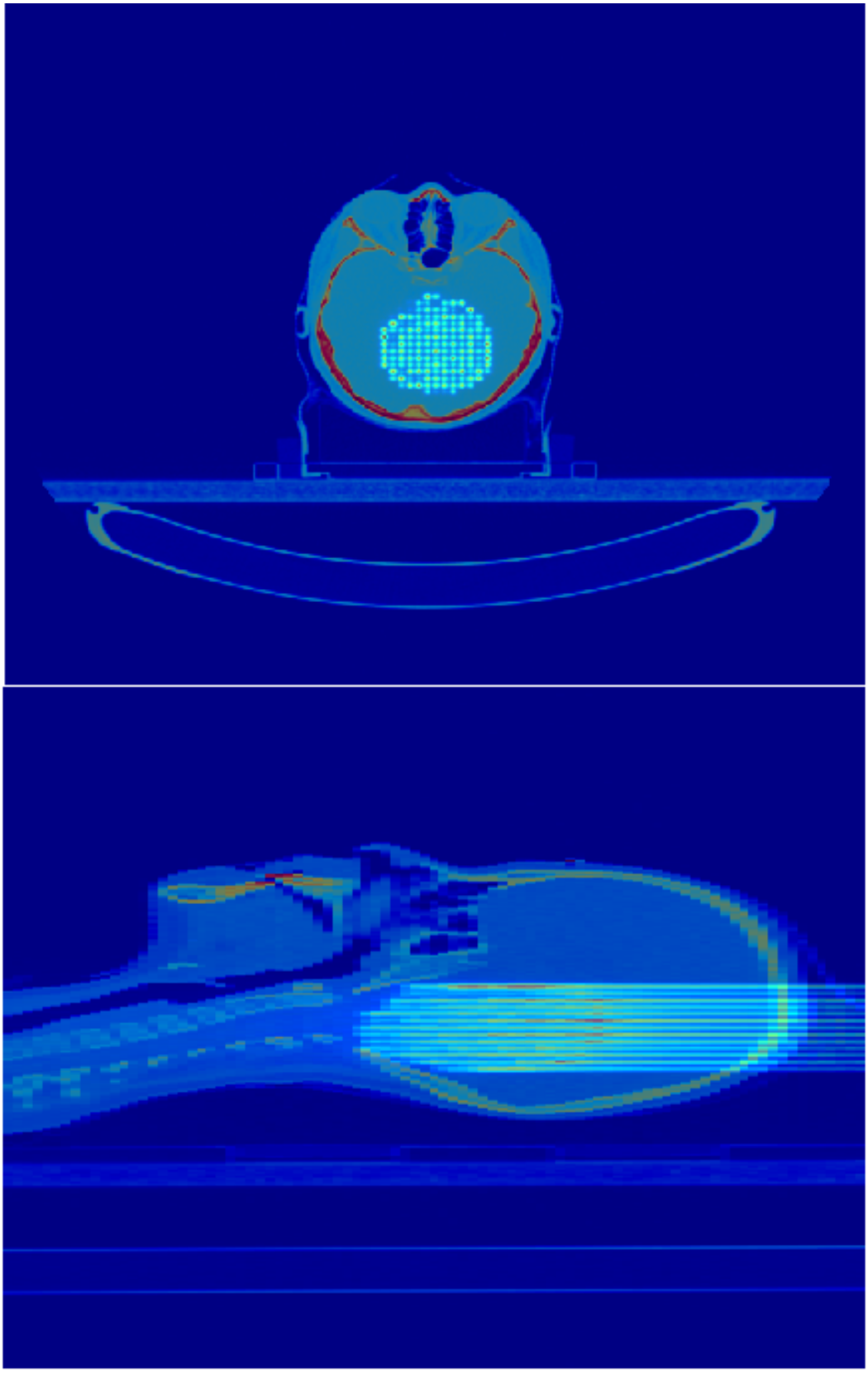

Figure B.1: Dose delivered to the patient with carbon ion therapy, axial view on top and sagital view below.